Formation and dispersal of pyroclasts on the Moon: indicators of lunar magma volatile contents.

Cerith Morgan[1], Lionel Wilson[1,2,*] and James W. Head[2]

[1]Lancaster Environment Centre, Lancaster University, Lancaster, LA1 4YQ, U.K.

[2]Department of Earth, Environmental and Planetary Sciences,
Brown University, Providence, RI 02912 USA

*Corresponding author
email address: l.wilson@lancaster.ac.uk

Highlights

- Vacuum conditions make explosive eruptions on the Moon very different from those on Earth
- Volatile release patterns in lunar magmas determine pyroclast size distributions
- Predicted pyroclast size distributions are similar to those in Apollo samples
- Pyroclast sizes interact with gas expansion in the vacuum to determine deposit characteristics
- The sizes of pyroclast deposits on the Moon imply a wide range of magma volatile contents

Abstract

We use new estimates of the total content and speciation of volatiles released during the ascent and eruption of lunar mare basalt magma to model the generation and behavior of gas bubbles, the disruption of magma at shallow depth by bubble expansion, and the acceleration and dispersal of the resulting pyroclasts. Lunar eruptions in near-vacuum differ significantly from those on bodies with an atmosphere: 1) exposure to near-zero external pressure maximizes volatile release to form gas bubbles; 2) the infinite potential expansion of the gas bubbles both ensures and maximizes magma fragmentation into pyroclastic liquid droplets with sizes linked to the bubble size distribution; 3) the speeds to which gas and entrained pyroclasts can be accelerated by gas expansion are also maximized. Generation of CO gas bubbles at much greater depths and pressures than bubbles of other volatiles produces bimodal (~120 and 650 microns) total pyroclast size distributions. In the near-vacuum, gas expands to pressures so low that gas-particle interactions enter the Knudsen regime, resulting counter-intuitively in the median grainsize in pyroclastic deposits first increasing, then decreasing, and finally increasing again with increasing distance from the vent, instead of decreasing monotonically as when an atmosphere is present. These complex gas-particle interactions cause clast size distributions to vary in a complex way with distance from the vent and the maximum thickness of the deposit to occur at about 75% of the maximum pyroclast range. Lunar eruptions typically evolve through four stages, which significantly influence gas release patterns. Most volatiles are released during the second, hawaiian-style eruption stage. However, elevated gas concentration can occur both in the short first stage (due to gas accumulation in the dike tip during ascent from the mantle) and in the third and fourth stages (due to reduced volume flux, increased time for gas bubble formation, growth, rise and coalescence, and strombolian activity replacing the hawaiian eruption style). Such gas concentration mechanisms can increase pyroclast ranges by a factor of ~5, but result in very much thinner deposits than if no concentration occurs. Maximum pyroclast range scales essentially linearly with total mass fraction of released volatiles; thus determination of the deposit radius around specific vents can provide data on lunar magma volatile contents. If the volatile inventory of the Apollo 17 orange glass bead picritic magma (~3400 ppm maximum) is typical, maximum ranges of the majority of pyroclasts would have been ~20 km. Such eruptions could explain 79% of the currently recognized pyroclastic deposits on the Moon. A few larger deposits and vents, such as the Aristarchus Plateau Dark Mantle and Cobra Head, suggest higher magma volatile contents. Numerous lunar vents show little evidence of associated pyroclastic deposits. Together, these observations suggest a wide range of volatile contents in lunar basaltic magma mantle source regions.

Keywords:
Moon
pyroclast dispersal
grain size
volatiles
explosive eruption
dark mantle
dark halo

1. Introduction

Since the earliest quantitative studies of lunar volcanism it has been clear that, although lunar mafic magmas were poor in volatiles relative to terrestrial equivalents (Housley, 1978), nevertheless the essentially zero atmospheric pressure on the Moon should have caused almost all lunar eruptions to have involved explosive activity at the vent (Wilson and Head, 1981). Although the initial magma ocean phase of lunar evolution may have been accompanied by a transient atmosphere, this quickly condensed and dissipated, well before the period of mare basalt volcanism (Shearer et al. (2006). The absence of a significant planetary atmosphere should have three main influences on a volcanic eruption. First, exposure to near zero external pressure maximizes the release of dissolved magmatic volatiles to form gas bubbles. Second, the negligible external pressure leads to extreme expansion of gas bubbles, ensuring that they become so closely packed that the thin liquid interfaces between bubbles collapse. This converts the the magma from a liquid containing gas bubbles to a gas entraining liquid droplets - the pyroclasts - whose sizes are linked to the bubble size distribution during this fragmentation process. And third, the speed to which gas and entrained pyroclasts can be accelerated by the expanding gas is also maximized. Additionally, the low acceleration due to gravity on the Moon enhances pyroclast dispersal, both directly via its control on the distance that a pyroclast ejected at a given speed can travel, and indirectly by producing a smaller lithostatic pressure gradient that allows more time for gas bubble expansion during magma ascent.

That explosive activity of the above kind had indeed taken place in many locations on the Moon was confirmed by the finding of pyroclastic glass beads in all of the returned Apollo regolith samples (Heiken et al., 1974; McKay et al., 1978; Arndt et al., 1984; Delano, 1986). The volcanic origin of these beads was confirmed by a comprehensive study of their petrologic and petrographic properties. Delano (1986) outlined the criteria to distinguish between glasses of pyroclastic and impact origin. The generally sub-mm sizes of these clasts (Figure 1) is consistent with theoretical predictions of the consequences of magmatic gas release in vacuum conditions (Wilson and Head, 1981). Spectroscopic surveys of the Moon have identified candidate pyroclasts mixed with the bedrock regolith in more than 100 locations, with 87 of these being characterized in detail (Gaddis et al., 2003; Gustafson et al., 2012). An understanding of the likely volatile species released from lunar magmas grew rapidly after the recognition of residual water in sampled pyroclasts (Saal et al., 2008; Hauri et al., 2011) and is an area of active research (Newcombe et al., 2017; Renggli et al., 2017; Rutherford et al., 2017). Global remote sensing surveys have been interpreted to mean that many lunar pyroclasts may retain up to ~300-400 ppm H_2O (Milliken and Li, 2017; Li and Milliken, 2017), likely as a result of being quenched as they left the hottest part of an expanding gas cloud (Head and Wilson, 2017). The retention of water in these amounts implies significantly higher amounts in the magma prior to eruption.

The volatile contents of the basaltic magmas associated with pyroclastic deposits are thought to predominantly reflect the composition of their mantle source regions. This is based on the fact that the magma source regions are typically deep, in excess of the several hundred kilometers (Shearer et al., 2006), and the fact that the dynamics of dike initiation and propagation favor very rapid ascent of the magma to the surface (Wilson and Head, 2017a). Only a very few surface vents and associated structures (Head and Wilson, 2017) suggest that dikes stalled at shallow depths and that volatile enhancement prior to eruption occurred at shallow depths: e.g., a distinctive deposit in Mare Orientale (Head et al., 2002) and vents associated with floor-fractured craters (Wilson and Head, 2018a).

The distances to which pyroclastic were ejected from lunar vents vary widely, from ~1 km to ~100 km (Gaddis et al., 2003; Gustafson et al., 2012). The inferred deposit volumes, ~0.5 km^3 (Trang et al., 2017) to ~500 km^3 (Campbell et al., 2008) cover such a wide range that it is likely that more than one mechanism was involved in their production. Thus, many of the smallest deposits, such as the 2-3 km diameter dark halo deposits inside Alphonsus, occur on the floors of impact craters and are likely to be the results of transient vulcanian explosions (Head and Wilson, 1979). These could have occurred when gases forming a few hundred ppm of the expelled mass accumulated at the tops of dikes intruded close to the surface of the crater floor breccia. These shallow dikes were a secondary effect of the intrusion of voluminous sills into the base of the breccia lens fed by dikes extending up from the deep mantle (Jozwiak et al., 2012, 2015; Wilson and Head, 2018a).

In contrast, the ~500 km^3 volume of the largest pyroclastic deposit (the Aristarchus Plateau; Campbell et al., 2008) is of the same order of magnitude as the volumes of the largest observed surface lava flows on the Moon (Head and Wilson, 2017), and is also similar to the volumes of lava implied to have been erupted during the formation of some sinuous rilles (Head and Wilson, 1981). These volumes, if from a single eruption, therefore suggest the near complete evacuation, in prolonged relatively steady explosive eruptions, of the magma from the largest dikes that can be formed in the deep mantle and ascend to penetrate the nearside lunar crust (Wilson and Head, 2017a). Further, the up to ~100 km pyroclast ranges implied by the lateral extents of the largest of these deposits (Campbell et al., 2008) require that clasts leave the vicinity of the vent at speeds of up to 400 m s^{-1}. Speeds this large have specific implications for the amounts of volatiles of a given composition released from the erupting magmas (Wilson and Head, 2017a).

Not all pyroclastic deposits on the Moon necessarily derive from long-lived steady eruptions. Figure 2a summarizes the sequence of events expected during a large-volume eruption on the Moon (Wilson and Head, 2018b). The opening phase (Figure 2b) can involve transient but unusually energetic ejection of pyroclasts as a result of the concentration of gas in the upper parts of dikes during their ascent from the mantle (Head et al., 2002; Wilson and Head, 2003; Wilson and Head, 2018b). The subsequent stages of large-volume eruptions are likely to involve steady hawaiian-style explosive activity (Figure 2c) followed by a transition (Figure 2d) to strombolian explosions in a lava lake filling the vent (Wilson and Head, 2018b), taking place with a low mean volume eruption rate of magma (Figure 2e). The concentration of gas into slugs rising though the dike magma, each one expelling part of the lake surface as it arrives there, can again generate bursts of pyroclasts powered by an enhanced volatile content.

In contrast to the near-vertical ejection of pyroclasts erupted into basaltic lava fountains on Earth (Head and Wilson, 1989), the absence of a significant atmosphere on the Moon causes the products of explosive lunar eruptions to be dispersed at a wide range of angles from vertical, forming structures similar in shape to the so-called "umbrella plumes" on Io (Strom et al., 1979, 1981; Glaze and Baloga, 2000), though much smaller in size. The very small sizes of lunar pyroclasts cause the resulting plumes (which are actually lava fountains) to be systematically more optically dense than lava fountains on Earth. High mass-flux eruptions of gas-poor magma form plumes with a very high particle number density, such that clasts cannot cool in flight except in a very thin shell at the outer edge of the fountain (Wilson and Head, 2017a). Only low mass flux eruptions of volatile-rich magma can produce a fountain which is sufficiently translucent to allow significant cooling of all of the pyroclasts. Many circumstances, therefore, are predicted to generate a molten lava lake surrounding the vent rather than a cold or partially cooled cinder- or spatter-cone, and the sizes of source depressions feeding many sinuous rilles appear to be consistent with the high mass flux, low volatile content scenario (Head and Wilson, 2017).

We now explore these issues by first estimating the size distribution of pyroclasts formed during a typical lunar explosive eruption and then using this to develop detailed models of the consequences of the three types of lunar explosive volcanism shown in Figures 2b, 2c and 2d-2e. We build on our earlier treatments of the volumes and eruption rates of lunar magmas (Wilson and Head, 1981; Wilson and Head, 2017a, Head and Wilson, 2017), use our new insights into the process of magma fragmentation under vacuum conditions (Morgan et al., 2019), and incorporate the consequences of varying amounts and compositions of lunar volatiles (Newcombe et al., 2017; Renggli et al., 2017; Rutherford et al., 2017). Our predictions form a basis for interpreting the data on pyroclasts collected during the Apollo missions (Heiken et al., 1974; Delano, 1986) and the inferences about lunar volatiles based on remote sensing observations (Milliken and Li, 2017; Li and Milliken, 2017), and also provide a framework for planning future sample collection missions.

2. Lunar pyroclast size distributions

Empirically, direct information on lunar pyroclast sizes comes entirely from the Apollo mission samples. Figure 1a shows mass distributions with size class reported for the Apollo 17 orange and black glass bead pyroclasts (Heiken et al., 1974; McKay et al., 1978; Arndt and von Engelhardt, 1987) and for green glass beads from Apollo 15 (Arndt et al., 1984). These authors note that only ~40% of the Apollo 17 orange glass droplets and ~49% of the Apollo 15 green glass droplets have a near-complete elliptical shape, implying significant breakage of these clasts. McKay et al. (1978) give detailed information on the relative proportions of undamaged, chipped, and broken glass droplets in the Apollo 17 orange glass samples. These are given in Table1, taken from the third part of McKay et al. (1978)'s Table 3, and show an increasing proportion of broken clasts with decreasing particle size. We return to breakage mechanisms later but here note that, although some droplets, both intact and broken, show tiny depressions surrounded by shock textures indicating that they have been impacted by hyper-velocity meteoroids, the vast majority of breakage events involved mutual collisions between droplets (Heiken et al., 1974). We therefore use the detailed information of McKay et al. (1978) on the Apollo 17 orange glasses to attempt to reconstruct the pre-breakage size distribution. Wittel et al. (2008) studied the expected break-up patterns due to collisions between brittle solid clasts and their Figure 7a shows that the largest and second-largest clasts produced in collisions at speeds of ~180 m s^{-1}, similar to those expected for the lunar pyroclasts, will have masses that are ~0.08 of the mass of the clast which has shattered. Thus, the original clast has a mass ~1/0.06 = ~12.5 times that of it largest fragments and, assuming all fragments have the same density, its diameter is ~$12.5^{1/3}$ = ~2.3 times larger than these fragments. Applied to the McKay et al. (1978) data, where the largest droplet diameter is close to 1000 microns, this implies that droplets with diameters up to ~2300 μm were likely present. Wittel et al. (2008), in their Figure 7b, also give the probability distribution of the masses of fragments, which follows a power law such that the number of a given mass is proportional to the mass to the power -1.9. Since the diameter is proportional to the cube root of the mass this implies that the mass distribution is proportional to the diameter to the power -1.9/3 = -0.63. Using this scaling, we have adjusted the size distribution of McKay et al. (1978): the broken clasts in each size class are distributed among all larger size classes in proportions weighted by the $(\text{diameter})^{-0.63}$ factor. This produces the distribution shown in Figure 1b. We stress that this reconstruction process is not unique, because we have had to estimate the size of the largest droplet that could possibly occur, and the volumes of the material collected in the Apollo samples do not contain enough large droplets to provide good statistics on the coarse end of the size distribution. Nevertheless, Figure 1b is probably a better approximation than Figure 1a to the initial size distribution created at the vent.

Although the sizes of pyroclasts shown in Figures 1a and 1b are qualitatively consistent with the expected extreme fragmentation of lunar magmas as they erupt into a vacuum (Wilson and Head, 1981), the distances between sample sites and their respective vents are unknown and, as we show later, neither the coarsest nor the finest parts of lunar pyroclast size distributions may have been sampled by any Apollo mission. We therefore attempt to predict the size distribution that pyroclasts would have had as they left the vent. To do this we require information on the release pattern of volatiles as magma ascends from great depth. We have used the volatile inventory proposed for the picritic magma forming the Apollo 17 orange glass beads analysed by Rutherford et al. (2017); the implications of using other authors' results are described in Section 5. Rutherford et al. (2017) found that up to ~1400 ppm CO would be released as pressures decreased below a value of ~200 MPa, corresponding under lithostatic conditions to depths greater than ~50 km, with very little being released at shallow depth, whereas release of up to ~1100 ppm H_2O, together with up to ~850 ppm sulfur and halogen species, would have taken place at depths less than 500 m, as shown in Figures 3a, 3b.

Since almost all of the CO is released at depths of at least ~50 km where the pressure is > 200 MPa, a major factor modifying the initial CO gas bubble diameters, likely to be ~5-10 μm (Masotta and Keppler, 2014), must have been decompression. We show in Section 3 that magma fragmentation will have taken place at a pressure of order 1 MPa, so that at this point CO bubbles will have had diameters of at least $[(200/1)^{1/3} \times (5 \text{ to } 10) =]$ ~30-60 μm. The rise speed of magma during the early phase of a large-volume, steady, explosive eruption on the Moon is likely to be ~5-10 m s^{-1} and the motion of the magma will be turbulent (Wilson and Head, 2017a). At this speed, magma will require ~1-3 hours to rise from ~50 km depth, allowing the opportunity for collisions between gas bubbles, especially near the walls of the dike where shearing is a maximum, increasing bubble sizes further. In contrast, the pattern of water release in lunar magmas is likely to be similar to that in terrestrial basalts, with a continuous pressure-dependent release between nucleation and fragmentation. The cumulative bubble size distribution can then be modelled as $N/N_0 = \exp[- \varphi /(G\ t)]$ where N is the total number per unit volume of bubbles of diameter φ and smaller per size class, N_0 is the initial number, t is the magma ascent time scale and G is the bubble radius growth rate (Mangan and Cashman, 1996). The relative number of bubbles of different sizes is $n(\varphi) = \mathrm{d}N(\varphi)/\mathrm{d}\varphi$. The bubble growth rates found by various authors differ considerably, from ~3×10^{-9} m/s for basalt containing 10 ppm water and being decompressed under static laboratory conditions (Masotta and Keppler, 2014) to 10^{-5} m/s inferred from basalt samples erupted in Hawai'i and initially containing ~10000 ppm water (Mangan and Cashman, 1996). Since the bubble separation in magmas must be proportional to the density of nucleation sites, and greater magma rise speeds favor supersaturation and high densities, we prefer growth rates comparable to those from Mangan and Cashman (1996) for lunar water release, but scale them by the total water content, resulting in a growth rate of ~5.5×10^{-7} m s^{-1}. Finally, we model the development of the bubble size distribution in CO based on the closest terrestrial analog, the release of CO_2 at pressures approaching ~400 MPa in basaltic magmas, where the radial growth rate of bubbles is ~6×10^{-8} m s^{-1} (Sarda and Graham, 1990).

We assume that as both populations of bubbles collapse during magma fragmentation the magmatic liquid deforms under surface tension forces to form pyroclastic droplets with diameters ϕ comparable to those of the bubbles - simple geometry shows that the ratio would be 0.97 for perfect cubic packing. We then multiply the number distribution of pyroclasts by the volume of each size class and, since all of the droplets have essentially the same density, this yields the mass distribution. Using the above bubble growth parameters, we find the very bimodal pyroclast mass distributions for droplets shown in Figure 4, with the modes for droplets produced from H_2O and CO bubbles occurring at sizes differing by a factor of ~30. However, the fragmentation of a liquid containing a complex bubble size distribution is influenced by both the size distribution and total vesicularity. Models developed for metal foams (Smorygo et al., 2011) involve inversion geometry to determine the liquid volumes between bubbles by defining a network of struts and nodes. The nodes become the pyroclasts after fragmentation, as shown in Figure 5 for a >90% vesicular hawaiian reticulite. This hawaiian sample contains a range of bubble sizes, with the ratio of the largest to the smallest being comparable to the ratio implied by Figure 4. Application of these strut-node ideas to the present case then suggests that from 3 to 5 of the smaller bubbles will be present in any node created by the larger bubbles and, depending on which struts fail first, what would have been a single large droplet from the CO framework becomes 3 to 5 smaller droplets. Applying this reasoning to Figure 4, we derive the mass vs. size distribution of Figure 6. The possibility that lunar pyroclast size distributions might be polydisperse (multiple sizes) rather than monodisperse (single size) was suggested qualitatively by Wilson and Head (2017a). The present quantitative analysis of the great disparity between the initial release depths of CO and all other volatiles implies that the distributions are essentially bidisperse (predominantly two sizes).

Comparison of Figure 6 with the reconstructed Apollo data in Figure 1b shows that the Apollo 17 droplet size distributions extend to smaller sizes than predicted. This is not surprising given the data on the proportions of broken beads in Table 1. If similar proportions occur at smaller sizes, the fine tail of the observed distribution is easily understood. Comparing Figure 6 with Figure 1b also shows that the predicted size distribution has a larger proportion of the distribution at sizes around 1 mm than the reconstructed observed distribution, but this is not surprising in view of the non-uniqueness of the reconstruction method we have used. Nonetheless we consider Figure 6 to be the best approximation that we can produce to a typical size distribution of lunar pyroclasts leaving the vent. We now use this to model pyroclast dispersal from the main phase of a lunar eruption, the equivalent of steady, hawaiian style lava fountaining (Wilson and Head, 2017a, 2018b) shown in Figure 2c. Subsequent Sections 4 and 5 deal with the two types of non-steady explosive activity under lunar conditions shown in Figures 2b and 2e, respectively.

3. Steady explosive eruptions

Long-lived explosive eruptions on the Moon (Figure 2c) had much in common with hawaiian-style lava fountain eruptions on the Earth (Head and Wilson, 1989) apart from the modification of the fountain due to its discharge into a vacuum rather than an atmosphere (Head and Wilson, 2017). In particular, magma fragmentation into pyroclasts will have begun when the volume fraction of gas bubbles in the magma became so large that the struts of the strut-node configuration shown in Figure 5 became unstable under the shearing forces imposed by the magma motion (Gonnermann, 2015). This is commonly modeled for terrestrial magmas by assuming a fixed critical volume fraction of gas bubbles irrespective of their sizes, with assumed values ranging from 0.7 to 0.8. We attempt to improve on this assumption using the treatment of Farr and Groot (2009) who analyzed the maximum packing of spheres with bi-modal size distributions like the one we have found. Farr and Groot (2009, their Figure 6) show the maximum volume fraction of a space that can be occupied by spheres as a function of the ratio of the modes and the relative volume fraction of the larger spheres. Our Figure 6 has size modes at ~120 and 650 microns implying a bubble size ratio of ~5.4. The heights of the two peaks, which are proportional to the volumes of small and large bubbles, are 13.5 and 12.5, implying a large bubble volume fraction of 0.48. Using Farr and Groot (2009)'s Figure 6 these values lead to a predicted maximum bubble packing of ~0.74. The increase in gas bubble volume fraction as the magma ascends through the sequence of events on Figure 3 is shown in Figure 7. The curve labeled 3400 is for the picritic magma analyzed by Rutherford et al. (2017), which would have released a maximum total volatile amount of 3400 ppm; the other curves show the equivalent information for magmas containing one half and one quarter of this amount of volatiles, corresponding to other compositions discussed in Section 5. The broken horizontal line indicates the 0.74 total bubble volume fraction at which magma fragmentation occurs.

We use the 0.74 maximum bubble packing fraction criterion for magma fragmentation to derive the relationship between the amounts of magmatic volatiles released and the kinetic energy available to accelerate gas and pyroclasts after fragmentation has occurred. Figure 7 shows conditions as a function of depth below the surface. Depth can be related to magma pressure using the assumption, discussed by Wilson and Head (1981), that the pressure in magma erupting steadily through a dike is in approximate equilibrium with the local lithostatic pressure in the host rocks. The depth range between the surface and the level at which CO is first released, taken for convenience as exactly 50 km, is divided into 10 m increments and the data underlying the volatile release patterns of Figure 3b are used to specify the amount $n_{i,k}$ of the kth volatile component which has been released by the time that the magma has risen to the ith depth level where the pressure is P. If the molecular mass of the kth volatile is m_k, the partial volume of that gas is

$$v_{i,k} = \frac{\left(n_{i,k}\, Q\, T\right)}{\left(m_k\, P\right)} \tag{1}$$

and the partial volume occupied by all of the gas species together is

$$v_{i,g} = \left(\frac{Q\,T}{P}\right) \sum_k \frac{n_{i,k}}{m_k} \tag{2}$$

where T is the magma temperature, taken as 1700 K, within the range of liquidus temperatures of lunar mare basalts (e.g. Williams et al., 2000), and Q is the universal gas constant, 8.314 kJ kmol^{-1} K^{-1}. The partial volume of the liquid is

$$v_{i,l} = \left(1 - \sum_k n_{i,k}\right) \Big/ \rho_l \tag{3}$$

where ρ_l is the liquid magma density. If now fragmentation occurs at a pressure P_f when the gas volume fraction is F, we have

$$F = \frac{v_{i,g}}{v_{i,g} + v_{i,l}} \tag{4}$$

and substituting from equation (2) and (3) and simplifying,

$$P_f = \left[\left(\frac{1 - F}{F}\right) \left(Q\, T\, \rho_l \sum_k \frac{n_{i,k}}{m_k}\right)\right] \Big/ \left(1 - \sum_k n_{i,k}\right) \tag{5}$$

Prior to magma fragmentation, the progressive release and expansion of the volatiles will have accelerated the rising magma to some extent, largely offset by the losses due to wall friction (Wilson and Head, 1981), and at the level where fragmentation begins the likely rise speed of the magma, U_0, will be of order 10-20 m s^{-1} (Wilson and Head, 2017a). As fragmentation occurs the bulk viscosity of the mixture of pyroclasts and gas rapidly approaches that of the gas phase and friction losses become small (Wilson and Head, 1981). The subsequent expansion of the volatiles initially takes place in an optically dense fountain (Wilson and Head, 2017a) so that the magma droplets, which represent almost all of the mass, are in good thermal contact with the gas. We therefore treat the system as a pseudo-gas, as suggested for eruptions into a vacuum by Kieffer (1982). Note that, because almost all of the clast acceleration takes place in the optically dense part of the eruption fountain, the acceleration process is completely decoupled from the external thermal environment, and there should be no difference between eruptions that take place during the 2-week-long lunar day and equally long lunar night.

Let the mass fraction of the kth volatile at the point of fragmentation be $n_{f,k}$. Then the kinetic energy per unit mass, E, available to accelerate the gas and clasts as the pressure decreases from the fragmentation pressure P_f to a lower value P_K is given to a good approximation by

$$E = \frac{\gamma\, Q\, T}{\gamma - 1} \sum_k \frac{n_{f,k}}{m_k} \left\{ 1 - \left(\frac{P_K}{P_f} \right)^{(\gamma-1)/\gamma} \right\} \tag{6}$$

Here γ is the effective ratio of the specific heats of the pseudo-gas, equal to $(s_{sp} + \alpha\, s_r) / (s_{sv} + \alpha\, s_r)$, where s_{sp} and s_{sv} are the specific heats at constant pressure and constant volume, respectively, of the gas, s_r is the specific heat at constant volume of lunar basalt, ~1500 J kg^{-1} K^{-1} (Williams et al., 2000), and α is the ratio $[(1 - n_t) / n_t]$, where n_t is the total mass fraction of released gas, $\Sigma n_{f,k}$. The specific heats at constant pressure and volume of the gas are taken as mass-fraction-weighted averages of the component species, using data from Kallmann-Bijl (1950), Harr et al. (1984), Kaye and Laby (1995) and NIST (2018). We find that, because the volatile content of lunar magmas is small, the thermal properties of the pseudo-gas are dominated by those of the pyroclasts, so that whatever detailed gas mixture is assumed, γ always has a value very close to 1.001, and the energies calculated from equation (6) are almost identical to those that would be found by assuming that the temperature remained constant at its initial value T.

In earlier treatments of lunar explosive eruptions (Wilson and Head, 1981; Wilson and Head, 2017a) it was assumed that P_K was the pressure at which an inferred mean pyroclast size of 300 μm entered the Knudsen regime. This occurs when the pressure becomes so low that the mean free path of the gas molecules, λ, is comparable to the diameter, ϕ, of the pyroclasts and the frictional interaction between clasts and gas requires major modification. This is expressed in terms of the Knudsen number, Kn, defined by

$$Kn = \frac{2\,\lambda}{\phi} \tag{7}$$

where the mean free path is given by

$$\lambda = \frac{2^{1/2}\, Q\, T}{3\, \pi\, d^2\, A\, P} \tag{8}$$

Here d is the effective diameter of a molecule, generally between 3×10^{-10} and 4×10^{-10} m (Kaye and Laby, 1995), and A is Avogadro's number, 6.0225×10^{26} kmol^{-1}. When Kn is comparable to or greater than unity, the terminal velocity of a clast through the gas, u_t, is given by

$$u_t = C_c \left(\frac{\phi^2 \, \sigma \, g}{18 \, \mu_g} \right) \tag{9}$$

where σ is the pyroclast density, g is the acceleration due to gravity, μ_g is the gas viscosity, and the normal expression is multiplied by the Cunningham correction factor, C_c, given by

$$C_c = 1 + Kn \,[2.34 + 1.05 \, exp(-0.39/Kn)\,] \tag{10}$$

Thus, when Kn is large, C_c is large, and the effective terminal velocity of a pyroclast in the gas is also large; this is the equivalent of saying that the clast no longer experiences any interaction with the gas and continues on a ballistic trajectory with the velocity that it has when this decoupling occurs. In our earlier work (e.g., Wilson and Head, 2017a), we adopted the mean lunar pyroclast size of 300 μm derived from an analysis in Wilson and Head (1981); we also assumed slightly different proportions of CO and the other gas components based on information available at that time (e.g., Sato, 1977), and found that P_K was about 90 Pa.

We adopt a similar treatment here; however, now that we have a detailed estimate of the expected pyroclast size distribution, we are able to take much more detailed account of the consequences of clasts decoupling from the expansion of the gas. There are two circumstances in which this happens. The first relates to relatively large clasts. For the Moon, with magma rise speeds, and hence gas speeds immediately after fragmentation, of 10-20 m s^{-1} (Wilson and Head, 1981), equation (9) shows that "large" implies clasts greater than ~10 mm in diameter. These will always have a significant terminal velocity in the gas; they never acquire a large fraction of the vertical gas speed, and generally fall to the ground within a few hundred meters of the vent. However, Figure 6 suggests that in steady hawaiian-style lunar eruptions such clasts are extremely rare, though they should become important in the strombolian explosive eruptions treated in Section 4. The second circumstance for steady eruptions relates to the smallest clasts. Equations (7) and (8) show that for any given gas pressure and temperature, and hence any given mean free path, it is the smallest clasts that have the largest Knudsen numbers and hence the largest Cunningham corrections, and so these begin to decouple from the gas before the larger clasts.

To quantify these issues, we use a spreadsheet program to follow the expansion of the gas, after its release at fragmentation, in accordance with equation (6) using a series of pressure decrements such that the pressure at each step is a fixed fraction of the previous value: 80% provides sufficient resolution. The gas temperature is kept constant in view of the buffering effect of the hot pyroclasts. This means that the gas viscosity, being mainly temperature-dependent (Kaye and Laby, 1995), can also be treated as constant, but the gas density and the mean free path of the molecules both change as the pressure decreases. The velocity of the gas and all of the clasts that have not yet decoupled from interaction with the gas is incremented in accordance with the energy increment for the current pressure reduction step. We divide the pyroclast size distribution of Figure 6 into 9 bins, with the ratio of upper to lower size limits set to 2. The vertical broken lines in Figure 6 show the boundaries of these bins, which are centered on pyroclast diameters of 10, 20, 40, 80, 160, 320, 640, 1280 and 2560 microns. For each bin size we follow the interaction of the clasts in that bin with the gas, evaluating Kn and C_c as the gas expands. As each bin size passes through the region of Kn = 1 to 2 the clasts effectively lose contact with the gas and cease accumulating further increments of velocity. As a result, the effective gas mass fraction that is accelerating the remaining clast sizes becomes larger, and the appropriate multiplication factor, $[1/(1 - f_l)]$, where f_l is the cumulative mass fraction lost so far, is applied to the energy increments and hence velocity increments in the subsequent expansion. This process is repeated as each clast size bin decouples. The gas velocity at which this occurs is recorded and the subsequent ballistic ranges of the clasts are found by evaluating the vertical and horizontal velocity components for a range of angles, θ, from the vertical extending to a maximum value, θ_l. The vertical clast velocity is obtained in each case by subtracting the terminal velocity of the clast from the vertical component of the gas velocity. Computational models of the expansion of supersonic gas jets (Wang and Peterson, 1957) imply that, for the very large pressure reduction ratios typical of the expansion of volcanic gases into a vacuum, θ_l = 65° is a suitable choice of limiting angle. All of the processes determining the final clast velocity take place in a relatively small region above the point in the magma conduit where fragmentation begins: clasts with diameters 20, 40, 80, 160, 320, 640, 1280 and 2560 microns decouple from the gas expansion at distances of 140, 192, 262, 357, 485, 653, 866 and 1012 m, respectively, above the magma fragmentation level, i.e., essentially within 1 km of the vent, and the temperatures of the expanding gas and pyroclasts decrease by about 20 K from their assumed initial value of 1700 K during this process.

Figure 8 shows the resulting maximum clast ranges. The smallest (~20 μm) pyroclasts in the distribution reach ranges of ~12 km and the largest which are present in significant amounts (~3000 μm) reach ranges of 5 km. However, intermediate-sized clasts (~600-1000 μm) reach ranges close to 20 km. This counter-intuitive result, that mid-sized clasts travel further than smaller ones, is the result of the smallest particles decoupling first from the still-expanding gas, thus allowing the larger clasts to benefit from the effectively greater gas mass fraction that acts on them and the consequent increased speed that they acquire. However, for the very largest clasts present, ~2500 μm in size, the fact that they have large terminal velocities in the gas becomes the dominant factor, and they fail to reach high speeds and fall close to the vent. This pattern of size sorting predicted in eruptions on the Moon is due entirely to the very low gas density involved during the late stages in the acceleration of the pyroclasts to their greatest speeds, and is applicable also to Mercury, Io, and the differentiated asteroids. It is in striking contrast to how sorting operates in explosive eruptions on planets with atmospheres like Earth and Mars. There, the consequence of large clasts having large terminal velocities in the gas is also present and controls the sorting by distance from the vent for the largest clasts (Wilson, 1999), but the sorting of intermediate-sized and small clasts occurs through the interaction between the turbulent convecting eruption cloud which is allowed to form by the presence of the atmosphere and the subsequent effects of the atmospheric wind regime. This always leads to a monotonic decrease in maximum clast size with distance from the vent, well-documented for Earth (Carey and Sparks, 1986; Wilson and Walker, 1987), inferred for Mars (Wilson and Head, 2007; Kerber et al., 2013), and fundamentally different from what is found here for the Moon.

More important than the maximum ranges reached by clasts of various sizes, shown in Figure 8, is the distribution with distance from the vent of the clasts in a given size class, controlled by the angle from the vertical, θ, at which the clasts are launched. The distribution is obtained by assuming that the spatial distribution of clasts in the jet of clasts and gas emerging from the vent is uniform. Then the mass of clasts ejected into any narrow range of angles from the vertical of width $d\theta$ is proportional to $\sin \theta \, d\theta$ (Glaze and Baloga, 2000). These clasts reach the ground at a range R defined by their eruption speed as described earlier and form one of a series of annular deposits each of whose width dR is determined by $d\theta$. The area of each annulus is ($2 \pi R\, dR$) and the thickness of the deposit formed is therefore proportional to [($\sin \theta\, d\theta$) / ($2 \pi R\, dR$)]. The classic case of completely ballistic ejection of clasts at speed V leads to the relationship $R = (V^2/g) \sin 2\theta$ where g is the acceleration due to gravity, giving the maximum range when $\theta = 45°$. Differentiating the angular dependence, we see that $2 \pi R\, dR$ is proportional to $\sin 2\theta \cos 2\theta\, d\theta$. As a result, the deposit thickness is proportional to [($\sin \theta\, d\theta$) / ($\sin 2\theta \cos 2\theta\, d\theta$)]. This expression reduces to $1/[\cos \theta (\cos^2 \theta - \sin^2 \theta)]$ which becomes infinitely large when θ is equal to 45°, implying an extreme concentration of pyroclasts at the maximum range. In our case the fact that the vertical velocity component of each clasts is reduced by its terminal velocity means that the maximum range is reached by clasts launched at an angle smaller than 45°, but a singularity in deposit thickness is still predicted at the maximum range. In practice no stream of explosion products is as perfectly organised as these formulae assume; turbulence, shearing forces at the volcanic conduit wall, and inter-particle collisions all contribute to smearing the ranges reached by clasts in a given part of the initial gas-pyroclast stream. Evidence for these factors can be seen in images of the ring-shaped deposits from other explosive eruptions into vacuum conditions, e.g., the ~154 km diameter "dark ring" pyroclastic deposit (Head et al., 2002) in Mare Orientale on the Moon (Figure 9a) and the ~1000 km diameter sulfur deposit from the Pele plume on Io (Figure 9b). Although a clear concentration of material occurs around the maximum range, it appears to be spread over at least ~10% of the deposit radius. To avoid the singularity, and to mimic this range-smearing process, we calculate the relative thickness in the deposit by incrementing the angle θ from the vertical in 5° steps, so that the successive annuli in which the ejected mass of pyroclasts lands each have a finite area. Figure 10 shows the result for one pyroclast size class, 640 microns. At each distance from the vent there is a contribution from clasts ejected at angles closer to the vertical than the angle giving the maximum range, labeled "high-angle", and those closer to the horizontal, labeled "low-angle". The sum of these, "total", gives the contribution to the deposit thickness at each distance from the vent from 640 microns clasts. There is, as expected, a very significant peak as the maximum range is approached - note the logarithmic thickness scale.

The above process is repeated for each grain size class. Figure 11 shows the relative thicknesses contributed, as a function of distance from the vent, by 5 of the 9 clast size classes; the other 4 classes are omitted for clarity but all show similar trends. It can be seen that there are large differences in the thickness contributions. Two factors control this: first, Figure 6 shows that the size classes contain greatly differing masses of material; second, it is inevitable that clasts that reach a greater maximum range spread whatever mass they represent over a larger area and hence contribute less thickness. By taking the thickness contributions from all 9 size classes at a given distance from the vent we can construct the predicted grain size distribution at that range. Figure 12 shows this for 11 selected ranges, zero, 5, 8.13, 10.42, 12.65,13.76,15.1, 16.39, 18.05, 19.29 and 19.49 km. These range values are chosen to make sure that each plot includes the maximum contribution from one of the grain size classes. A number of important effects emerge. At ranges between ~5 and 9 km all clast sizes are present but there is a significant excess of clasts in the 2560 micron size range. At ranges between ~10 and ~15 km the size distribution is dominated by ~100 to 200 micron sized clasts. At ranges between ~15 km and the maximum range of ~20 km, the peak in the grain size distribution moves to coarser size fractions and becomes narrower, with ever more of the smaller clast sizes being entirely absent. The overall pattern is that with increasing distance from the vent the clast size distribution is dominated by first coarse, then fine, then intermediate, and finally again coarse particles. Given that most of the pyroclasts found in the Apollo samples are smaller than ~600 microns (Figure 1) this has the important implication that, if they were ejected in eruptions of magmas having volatile contents like those implied by the analysis of the Apollo 17 orange glass by Rutherford et al. (2017), they were collected at distances between ~10 and ~ 16 km from their respective vents. We note that, for the Apollo 17 site, Schmitt et al. (2019) have suggested that one of several linear clefts, located in the Sculptured Hills unit and containing concentrations of dark mantle material, may be a source vent for the orange glass pyroclasts collected at the Shorty crater site. The separation of these two locations is ~13 km, consistent with the above conclusion.

The final analysis step is to sum the thickness contributions to the deposit by the various grain size classes at a given distance from the vent to find the total thickness of the deposit. This is shown in Figure 13. In so far as the maximum deposit thickness occurs at about 75% of the maximum range this distribution bears a qualitative similarity to the examples shown in Figure 9, though in neither case is the match perfect. On the Moon, regolith formation mixes the pyroclasts with the underlying material, disguising the thinnest part of the deposit (Head and Wilson, 2020), whereas on the very active Io blanketing by later eruption deposits has a similar effect. We note that the area of the ~20 km radius deposit predicted by our analysis is ~1250 km^2. The combined data sets of Gaddis et al. (2003) and Gustafson et al. (2012) contain 87 proposed pyroclastic deposits of which only 18 have areas larger than 1250 km^2. Thus, eruptions of magmas with volatile inventories similar to that of the Apollo 17 picrites could explain ~80% of the currently recognized lunar pyroclastic deposits. We now consider mechanisms that might lead to more widespread clast dispersal.

4. Transient vent-opening explosive activity

Propagating dikes have a low pressure in the magma at their upper tips, which maximizes the pressure gradient required to drive the motion of the dike magma against wall friction (Lister, 1990a). Lister and Kerr (1991) and Rubin (1993) inferred that this tip pressure should be the pressure at which the most soluble magmatic volatile present (commonly water in magmas on Earth) is just saturated, and that the uppermost part of a dike will consist of an elongate cavity containing pure gas at this saturation pressure. Wilson and Head (2003) pointed out that there should be a zone of magmatic foam beneath the gas-filled tip cavity as volatiles exsolve to be in equilibrium with the local pressure gradient, and that as a result the tip pressure is likely to be that at which the maximum gas bubble packing density is reached, essentially the fragmentation criterion used in the previous section. As a propagating dike breaks the surface (Figure 2b), gas in a pure gas cavity will be erupted violently as its pressure is released, but will carry no pyroclasts with it, though it may locally redistribute some regolith clasts (Head and Wilson, 2017). Release of the magmatic foam beneath the pure gas cavity will essentially mimic the explosive activity modelled in Section 2, because little relative movement of gas bubbles and magma will have occurred during the rise of the dike through the lithosphere, which Wilson and Head (2017a) show will take only a few hours on the Moon.

However, if a dike approaches very close to the surface but does not immediately erupt, then the pressure distribution within it will adjust to the progressive relaxation, as the dike decelerates to rest, of the pressure gradient previously driving the magma motion. After the dike comes to rest, gas bubbles begin to drift upward buoyantly through the magma. Particularly important in the lunar case, bubbles of CO released at ~200 MPa pressure, i.e., about 50 km depth (Rutherford et al., 2017), will then drift upward through the magma to accumulate at shallow depth. As this happens, the pressure in the dike tip rises and, if it becomes large enough, a fracture will propagate to the surface initiating an eruption (Head and Wilson, 2017; their Figure 6). Consider a case where CO bubbles have drifted upward so that all of the CO which has been released at depths shallower than 50 km is concentrated in the upper 25 km of the dike. The effective CO content will have increased from 1395 ppm (see Figure 3) to 2790 ppm. Figure 14 shows the excess pressure in a dike containing magma with a density of 2950 kg m^{-3} (Kiefer et al., 2012) extending 40 km into the mantle beneath the 30 km thick nearside crust of the Moon. The hydrostatic pressure in the crust is modeled assuming a crustal rock grain density of 2930 kg m^{-3} (Kiefer et al., 2012), a surface porosity of 24%, and an exponential decrease of pore space with depth with a e-folding constant of 1.18×10^{-8} Pa^{-1} (Head and Wilson, 1992). The mantle density is assumed constant at 3250 kg m^{-3} (Wieczorek et al., 2013). These assumptions yield pressures of 334.6 MPa at the dike base and 124.0 MPa at the crust-mantle boundary and a mean crustal density of 2550 kg m^{-3}, in agreement with the value estimated by Wieczorek et al. (2013). The dike magma is assumed to be in equilibrium with the host rocks at its bottom edge; the internal excess magma pressure then reaches a maximum of 19.4 MPa at the crust-mantle boundary and is 9.2 MPa at the surface. When the overlying crust fails and this magma is erupted, it will release the 2790 ppm of CO together with all of the other five volatiles shown in Figure 3, which together amount to 2005 ppm, making a total of 4795 ppm. The eruption will be hawaiian in style because of the high gas content. However, the mass flux will not be high because the dike that is being evacuated has already reached an equilibrium configuration around the crust-mantle boundary and by this time will be closing slowly as a result of the action of the lithospheric tectonic stress. The maximum range of pyroclasts is proportional to the square of their eruption velocity, in turn proportional to the kinetic energy per unit mass of the erupting mixture, which equation (6) shows is proportional to the sum of the gas mass fractions. With the effective gas content of the erupting materials having now increased from (1395 + 2005 =) 3400 ppm to 4795 ppm, all of the clast ranges in Figure 8 will, to a good approximation, be increased by the factor (4795/3400 =) 1.41 during this activity, making ranges up to ~28 km common. In a more extreme example, assume that the CO is concentrated into the upper 16.7 km of the dike, representing a three-fold concentration to 4185 ppm. The dike tip pressure in this case is 10.8 MPa when the overlying crust fails and the initially erupting magma contains (4185 + 2005 =) 6190 ppm gas; the ranges of Figure 8 are increased by a factor of (6190/3400 =) 1.82, making values up to 36 km common.

Clearly, gas concentration in rising dikes can significantly increase the extent of pyroclast dispersal. However, only that part of the magma in the region of gas concentration will be involved in the process. If any of the rest of the magma in the dike erupts it will do so with a reduced volatile content. For the two cases just described, when gas is concentrated into the upper 25 km of the dike, 30% of the magma volume is gas rich and 70% is gas-depleted. When gas is concentrated into the upper 16.7 km of the dike, 12% of the magma volume is gas rich and 88% is gas-poor. In cases like this the maximum range of pyroclasts would decrease dramatically as the change from the gas-rich to the gas-poor stage of the eruption occurred. Also the essential absence of the CO component would mean that the peak at ~ 700 microns in the clast size distribution of Figure 6 would shrink, leaving a monodisperse distribution with its peak near 100 microns.

An example of extreme gas concentration on the Moon leading to a limited magmatic eruption is the near-circular, ~154 km diameter "dark ring" pyroclastic deposit in Mare Orientale (Figure 9a). Head et al. (2002) proposed that this deposit was the result of an extremely energetic explosive eruption triggered by the accumulation of gas at the top of a dike intruded to shallow depth. In this rare case the dike was sufficiently wide that significant convection of its magma occurred over an ~20 month period while the dike was cooling. This allowed almost all of the magma in the dike to be cycled multiple times to shallow enough depths and hence low enough pressures that its volatiles were released. Failure of the retaining crust was estimated in this case to occur when the pressure in the dike tip reached a value slightly greater than 10 MPa, approaching the limit imposed by the likely tensile strength of the overlying crustal rocks.

The most extreme example of pyroclast dispersal on the Moon is the deposit (no. 1 in the catalog of Gaddis et al., 2003) that blankets the Aristarchus plateau. With an estimated radius of ~125 km, the implied magma volatile mass fraction is 6.25 times greater than the 3400 ppm adopted as typical here, 21,250 ppm, i.e., 2.125 mass %, greater than is typical of basalts on Earth. Equation (6) shows that if the released gas is dominated by low molecular weight species, then a smaller magma volatile content is needed to enable a given range to be reached. Thus, if H_2O were the only volatile, the amount implied by the 125 km range is reduced to 1.22 mass %, still large by terrestrial standards. However, the Aristarchus deposit is unusual in several respects, not least the presence, near the center of the deposit, of the Cobra Head source of Rima Schröter, the largest lunar sinuous rille, and a prominent hill likely composed of pyroclastic materials (Jawin et al., 2016). It would not be entirely surprising if it were the eruption site of unusually volatile-rich magma.

We now explore a second type of non-steady explosive volcanic activity that can lead to effective gas concentration in explosion products, leading to unusually great dispersal.

5. Strombolian explosive activity

The term strombolian in relation to explosive activity on Earth covers a range of circumstances, as discussed, for example, by del Bello et al. (2012) and Gaudin et al. (2017). The common theme is the concentration of gas from a given volume of magma into a small part of that magma volume so that the effective gas content of the small volume is increased. The concentration process may be dominated by the differential rise speeds of gas bubbles within the dike magma when the rise speed of the magma is sufficiently small to allow time for larger bubbles to overtake and coalesce with small ones (Parfitt and Wilson, 1995; Parfitt, 2004). Alternatively, the process may be encouraged by interruptions of the smooth flow of magma due to complexities in the geometry of the margin of the dike (Vergniolle and Jaupart, 1986; Jaupart and Vergniolle, 1988, 1989). Commonly, the gas concentration process causes coalescence of gas bubbles into ever larger bubbles which, as they grow and accelerate, evolve from a sub-spherical shape to become Taylor bubbles with rounded tops and flattened bases (Davies and Taylor, 1950). The final stage of this process involves the Taylor bubbles coalescing into very elongate slugs (Hasan et al., 2019) which almost fill the width of the conduit connecting the dike to the surface vent (Figure 15). The slugs rise through the magma which is itself rising through the conduit to feed a lava lake that may overflow to feed lava flows (Wilson and Head, 2018b). Emergence of each gas slug through the surface of the lava lake then leads to the disruption, by tensile and shearing forces, of the film of lava immediately above the top of the slug and the subsequent acceleration of the lava clots produced. Because the ratio of the mass of gas in the slug to the mass of expelled lava is high, the result is an energetic explosion, but such explosions are intermittent; on Earth there can be significant time intervals, from tens of seconds to hours, between the appearances of successive slugs (Taddeucci et al., 2015).

In the case of lunar eruptions of this type (Figure 2d) we have CO being released at what are by terrestrial standards very great depths and most other volatiles being released at shallow depths (Rutherford et al., 2017). The longer travel time of both magma and CO bubbles from the greater depths on the Moon, especially towards the end of an eruption when the magma rise speed is expected to be low (Wilson and Head, 2018b), allows more time for mutual bubble interactions, especially bubble coalescence and growth. As a result, we may expect lunar strombolian eruptions to involve large gas slugs dominated by CO and to be unusually energetic. Furthermore, whereas the magma clots ejected in explosions on planets with significant atmospheres quickly reach equilibrium with the atmospheric pressure, no such equilibrium is reached when the atmosphere is absent, and ongoing nucleation of new gas bubbles leading to continuing fragmentation of the ejected magma clots is expected to occur. This adds water and other late-released volatiles to the copious CO from the slug, increasing the acceleration of the pyroclasts, which we expect to have a range of sizes similar to that shown in Figure 6. In order to simulate strombolian explosions on the Moon we require a model that has the flexibility to allow us to vary the mass of gas in the slugs and the conditions at the surface of the lava lake through which the slugs emerge. The model developed by del Bello et al. (2012) is well-suited for this, in that the pressure at the surface of the lava through which the slug emerges is a major factor in determining the scale of the explosion. We therefore need to consider the conditions at the surface of a lava lake on the Moon (Figure 2d).

Any lava exposed to the vacuum at the lunar surface will attempt to exsolve almost all of its volatiles and vesiculate (Fielder et al., 1967; Wilson and Head, 2017b), but the conditions under which it arrives at the surface are important. In Section 3 we dealt with steady hawaiian eruptions where magma rose to the surface at high speed, ~10-20 m s^{-1} (Wilson and Head, 2017a), began vesiculating at a few hundred meters depth, and fragmented at shallow depth into a high-speed gas-pyroclast mixture dispersed over many kilometers. In lunar strombolian activity we are dealing with magma rising slowly, at less than 1 m s^{-1} (Wilson and Head, 1981, 2018b) (Figure 2a), and containing much less gas because all of its CO is now concentrated into slugs which may well have scavenged some of the other volatiles from the magma sheared against the conduit walls by the passage of slugs (Suckale et al., 2010; Pering and McGonigle, 2018). Wilson et al. (2019) estimate that as much as 80% of the non-CO volatiles could be scavenged into the slug as it nears the surface. Figure 3 shows that removal of the CO into slugs would cause the lava rising into the lake in the vent to contain a total of 2005 ppm gas with a mean molecular mass of 33.7 kg $kmol^{-1}$; slug scavenging of ~80% of this would leave ~400 ppm in the lake magma. The equivalent of the analysis in Section 2 shows that this magma would begin to fragment at depths up to 60 m ejecting typical pyroclasts to a height of ~800 m. However, because the lava in the lake is moving slowly, the stream of clasts and gas rising from the lake surface is subject to the influence of the pyroclasts falling back into the lake, and these exert a downward drag force on the rising gas. A balance is quickly reached in which there is effectively a fluidized bed separating the vesicular liquid in the lake from the overlying vacuum. A model of this type of system was developed by Wilson and Heslop (1990) to predict conditions in collapsed lava fountains feeding ignimbrite-forming eruptions on Earth and Mars. They showed that an equilibrium is reached in which the pressure at the level where the rising and falling particles are in balance is about half of the value that it would have if all of the pyroclasts escaped unhindered from the vicinity of the vent. Using equations (1) to (4) of Wilson and Heslop (1990) we show in Table 2 the equilibrium pressure, P_{lake}, the upward gas speed, U, the pyroclast rise height, H, and the clast travel time, τ, of 100-300 micron pyroclasts for a range of non-CO magma volatile contents, n_{lake}, up to 1000 ppm.

We now use the lava lake surface pressures, P_{lake}, in Table 2 as the reference pressures, i.e. as effective atmospheric pressures, for the del Bello et al. (2012) model of slug bursting. We implement the algorithm given by del Bello et al. (2012) in their Appendix B as a spreadsheet program in which the inputs are the conduit radius and the magma properties. We adopt 10 m for the conduit radius, a value consistent with the late stage of an eruption where the erupted volume flux is ~10^3 m^3 s^{-1} and the driving pressure gradient is ~20 Pa m^{-1} (see examples in Wilson and Head, 2017a). Appropriate magma properties are a temperature of 1700 K, a viscosity of 1 Pa s and a density of ~3000 kg m^{-3}. These values allow us to evaluate the properties of the gas slug using results given by Llewellin et al. (2012), who show that the dimensionless wall film thickness x, defined by

$$x = f / R \qquad (11),$$

where f is the thickness of the liquid film against the pipe wall and R is the conduit radius, a simple function of the dimensionless inverse viscosity of the liquid, N_f, defined by

$$N_f = [\rho_l \, (g \, D^3)^{1/2}]/\mu_l \qquad (12),$$

where D is the conduit diameter, ρ_l is the liquid density and μ_l is the liquid viscosity. For $N_f < 10$, x is independent of N_f and is ~0.33; in the interval $10 < N_f < 10^4$, x decreases sigmoidally with increasing N_f; and for $N_f > 10^4$, x is again independent of N_f and is ~0.08. For our 10 m radius conduit N_f is 3.41526×10^5, so that $x = 0.08$, the film thickness is $f = 0.8$ m, and the slug radius is 9.2 m. The rise speed of the slug, U_{slug}, is related to the Froude number Fr by (Llewellin et al., 2012)

$$Fr = U_{slug}/(g\ D)^{1/2} \qquad (13),$$

and Fr can also be related to N_f by

$$Fr = 0.34\ [1 + (31.08/N_f)^{1.45}]^{-0.71} \qquad (14),$$

so that in this case $Fr = 0.34$ and $U_{slug} = 1.935$ m s^{-1}.

A large number of parameters are generated by the algorithm of del Bello et al. (2012), of which the most important for our purpose are the pressure in the slug as it bursts, P_{slug}, and the ratio of the mass of gas released from the slug and the mass of magma ejected by it, i.e., the effective volatile content of the ejected material. The del Bello et al. (2012) treatment makes no assumptions about the lengths of slugs causing strombolian explosions and appeals to observations that clearly imply a range of values depending on the conduit geometry that is causing the segregation of gas into slugs. In the lunar case we are dealing with slugs forming spontaneously in the simple geometry of a dike extending sub-vertically for several tens of kilometers (Figure 15). We therefore appeal to both theoretical and observational analyses (Barnea and Taitel, 1993; Xia et al., 2009) that show that the most likely equilibrium length of a slug is ~14 times the diameter of the conduit through which it rises, in our case 20 m, making the most likely slug length ~280 m by the time the slug nears the surface. A remaining major unknown is how much of the lake lava immediately above the top of the slug will be entrained into the explosion process. At one extreme, all that will be ejected is a thin layer of lava of comparable depth to the thickness of the lava film smeared against the conduit walls by the passage of the slug, and this leads to a maximum effective volatile mass fraction in the ejected material, n_{max}. At the other extreme, in principle most of the column of lake lava immediately above the bubble as the stress of its arrival disrupts the lake surface might be ejected, leading to a minimum volatile content n_{min} in the ejecta. This would be the case if, for example, significant cooling and thickening of a lake crust had occurred, as appears to have been the case in the Ina caldera (Qiao et al., 2019).

Table 3 summarizes the results. Part (a) of the table corresponds to no overflow from the lake as the slug nears the surface, as would be the case if the lake were contained within a summit crater allowing the lake surface to rise without overflowing, and part (b) assumes copious lake overflow in cases where there is no significant retaining structure. In each part we give the pressure in the slug, P_{slug}, the length of the slug just prior to its bursting, L_{plug}, the maximum and minimum effective volatile contents of the ejecta, n_{max} and n_{min}, respectively, the corresponding ejection speeds, U_{max} and U_{min}, and the corresponding ranges, R_{max} and R_{min}, to which pyroclasts in the middle of the droplet size range could be ejected. The ranges should be compared with those of pyroclasts from the same magma, containing a total of 3400 ppm volatiles, erupting under steady hawaiian conditions, ~20.6 km. The very large spread in speeds and ranges reflects the potential great diversity of intermittent explosive volcanic activity (on all planets). However, for lunar strombolian explosions we are treating conditions at the end of an eruption, the early part of which may have developed an extensive lava lake around the vent (Wilson and Head, 2018b), and we consider it much more likely that part (a) of the table will be relevant. Furthermore, the entries (in parentheses) for a lake surface pressure of 2×10^5 Pa in the table are close to the limits of applicability of the del Bello et al. (2012) treatment and are of uncertain reliability. Finally, we consider that the low viscosities of lunar magmas make it very likely that magma will drain efficiently from the region above a slug nearing a lava lake surface and that conditions corresponding to the maximum pyroclast ranges in Table 3 are the more likely to occur, with values of at least 150 km.

Ejection of pyroclasts to 150 km would readily explain all of the large dark mantle deposits identified on the Moon, if they were indeed emplaced around a single vent. However, the extreme concentration of gas required to cause such extreme dispersal of these clasts puts constraints on the likely thicknesses of deposits that are even more severe than those implied by gas concentration events at the starts of eruptions described in Section 3. In modeling mantle magma sources feeding lunar eruptions, Wilson and Head (2017a, 2018b) showed that major eruptions on the Moon involved dikes with volumes of several hundred km^3 ascending rapidly from the deep mantle and erupting magma at very high volume fluxes for a few to several days in vigorous hawaiian-style eruptions (Figure 2c). A transition from hawaiian- to strombolian-style activity would then set in as the dike feeding the eruption reached an equilibrium configuration where the negative buoyancy of the dike magma in the crust was just compensated by the positive buoyancy of the dike magma in the mantle (Figure 2d). Given typical densities, this would imply the dike having approximately equal lengths above and below the density discontinuity at the crust-mantle boundary. With a nearside lunar crustal thickness of 30 km this implies that the horizontal and vertical extents of the dike, assuming a penny shape, would also be 30 km and its mean thickness would be ~30 m, so that its total volume at this point would be ~85 km^3. Rutherford et al. (2017) showed that lunar magmas were likely to release CO at all depths less than ~ 50 km, so only the magma in the bottom 10 km of the dike would still contain CO that could be released during convective overturn of the dike magma after the dike ceased rising. The assumed penny shape of the dike implies that this magma would represent 7.4% of the total dike volume, i.e., ~6.28 km^3. This volume, with a magma density of ~3000 kg m^{-3}, represents a mass of 1.9 x 10^{13} kg; if CO forms 1395 ppm of the magma by mass (Rutherford, 2017), the CO mass is 2.63×10^{10} kg.

The 280 m slug length used in our model implies that for lava lake pressures of 0.5×10^5, 1×10^5, 1.5×10^5 or 2×10^5 Pa the mass of CO in the slug would be 1.4×10^4, 2.0×10^4, 2.7×10^4 or 3.5×10^4 kg, respectively. Using 3×10^4 kg for illustration, eruption of all of the 2.63×10^{10} kg of CO requires 876,000 explosions. If the strombolian phase of the eruption lasts for ~6 months (Wilson and Head, 2018b), the interval between explosions is 18 seconds. If the magma expelled consists of only the 0.8 m thick film draining from the top of the slug as it emerges through the lake, the pyroclast volume per explosion is 251 m^3 and the total pyroclast volume expelled in the 876,000 explosions is 2.2×10^8 m^3. When only the 0.8 m thick film is expelled the effective volatile content of the exploding material is ~40,000 ppm (Table 3) and the maximum ejection distance is conservatively 150 km making the deposit area 7.1×10^{10} m^2. Deposition of 2.2×10^8 m^3 of pyroclasts over this area produces an average deposit thickness of 3.1 mm. Other eruption scenarios are possible. For example, if an unusually small volume dike (by lunar standards) were only just able to reach the surface, it could avoid the hawaiian eruption phase and erupt essentially all of its magma in the strombolian explosive mode. This would lead to all of the CO in the dike magma being available for use in generating a widely-dispersed deposit, and for the above dike geometry this would amount to 3.55×10^{11} kg of CO. A total of 11.8 million explosions would be needed to remove all of this gas and, spread over perhaps 1 year, explosions would take place at 2 to 3 second intervals. The total volume of magma expelled as pyroclasts to a maximum range of ~150 km would be ~3.0×10^9 m^3, and deposition of this over the 7.1×10^{10} m^2 deposit area would produce a deposit ~4.2 cm deep.

In summary, transient strombolian activity, likely to be common in the late stages of lunar explosive eruptions, has the potential to produce extremely widespread deposits extending out to ~150 km from the vent. However, it is extremely unlikely that these kinds of deposits would be detectable by remote observation techniques: pyroclast layers with thickness of mm to cm would be readily mixed into the existing regolith onto which they fell by primary and secondary impact cratering during the at least 1 Ga since their eruption (Speyerer et al., 2016; Costello et al., 2018; Head and Wilson, 2020).

6. Discussion

6.1 Pyroclast formation.

The predicted size distribution of lunar pyroclastic droplets developed in Section 2 is based on the assumption that the droplets are formed by a single process of disruption of the magmatic liquid by the expansion of gas bubbles. We discuss below how the initial size distribution may be modified by brittle processes after the droplets have cooled but consider here the possibility that, after formation and while still fully molten, droplets may break into smaller droplets as a result of hydrodynamic instabilities in the shape of the droplets induced by shearing forces due to their velocity, V, relative to the gas. Three dimensionless numbers control break-up under shearing forces (Jain et al., 2018), the Reynolds number, $Re = (\rho_g D V)/\mu_g$, the Weber number $We = (\rho_g V^2 \phi)/s$, and the Ohnesorge number, $Oh = \mu_g/(\rho_l \phi s)^{1/2}$, where ρ_g and μ_g are the density and viscosity of the gas, ρ_l is the density of the liquid, s is the surface tension of the liquid-gas interface, and ϕ is again the diameter of the clast. We calculated typical gas and pyroclast velocities and gas densities in Section 2; using these values, and consulting Jain et al. (2018, their Table 1), we find that hydrodynamic break-up is unlikely to be important for droplets smaller than ~10 mm. However, hydrodynamic break-up would quickly become very important for droplets larger than ~20 mm, perhaps explaining their absence from the Apollo samples.

6.2 Pyroclast dispersal.

The absence of any significant atmosphere on the Moon (and Mercury and Io) has multiple consequences for the dispersal of pyroclasts. The obvious ones are the release of a greater proportion of the magmatic volatiles and the greater expansion of the gas bubbles formed by the released volatiles. Together these factors cause the grain size distribution to be dominated by much smaller particles. Also, without an atmosphere it is impossible to form a convecting eruption cloud, the main mechanism of pyroclast dispersal on Earth (and probably on Mars and possibly on Venus). Less obvious is the finding that both the largest and the smallest pyroclastic droplets will decouple from the expanding volcanic gas stream earlier than intermediate-sized droplets, allowing the latter to reach the greatest ranges (Figure 8). This finding leads to characteristic variations with distance from the vent of both grainsize distribution (Figure 12) and deposit thickness (Figure 13). These have consequences for analyses (e.g., Li and Milliken, 2017; Milliken and Li, 2017) that need to assume a deposit grainsize to extract information from remote sensing data on residual water contents in lunar pyroclast deposits. Also, if enough samples from a long traverse across a pyroclast deposit were available for analysis, it might be possible to at least infer the direction, if not the distance, to the explosive vent. Thus, comparing Figure 1 with Figure 12 suggests that the Apollo 17 glass bead samples were closer to their parent vent than those at the Apollo 15 site.

6.3 Lunar magma volatile species.

Our numerical results are based on the volatile inventory inferred for the picritic magma forming the Apollo 17 orange glass beads analyzed by Rutherford et al. (2017). Other authors propose different amounts and species of volatiles released in explosive eruptions of lunar basalts. Thus, Newcombe et al. (2017) based their work on the Apollo 15 yellow pyroclastic glasses whereas Renggli et al. (2017)

also studied the Apollo 17 orange glasses. The analysis by Renggli et al. (2017) implies that nearly equal mixtures of CO, S_2 and H_2 are present at fragmentation with the molar proportion of H_2 increasing as the pressure subsequently decreases. Newcombe et al. (2017) predict that CO dominates until the pressure is less than ~1.5 MPa, when H_2 becomes dominant in terms of mole fraction. Just as for terrestrial magmas (e.g., Lowenstern, 2001; Edmonds and Wallace, 2017), the sequence in which the composition of a magmatic gas phase changes with decreasing pressure has profound implications for eruption dynamics and the transport of metals and trace volatiles. Figure 3 shows the magmatic mass fractions of the volatiles proposed by Rutherford et al. (2017) used in our calculations above. Renggli et al. (2017, their Figure 2b) give the magmatic mole fractions of the volatiles that they propose at 1773 K and 0.1 MPa pressure, close to fragmentation conditions. Newcombe et al. (2017, their Figure 11f) give the relative volume fractions of the gas species they propose at their 0.5 MPa fragmentation pressure and 1623 K temperature. The magma mole fractions of Renggli et al. can be converted to magma mass fractions using the appropriate volatile molecular masses. The relative volumes of Newcombe et al. can be converted to relative masses using their pressure and temperature values. With these conversions, Table 4 gives the mass fractions and molecular masses of the volatiles in the magma at fragmentation for each of the above three data sources, with the Renggli et al. and Newcombe et al. values scaled so that they yield the same maximum total magma volatile inventory, 3400 ppm, proposed by Rutherford et al. (2017). Table 4 also gives the values, for each source, of the quantity $\sum (n_{f,k}/m_k)$ needed in equation (6) to calculate pyroclast launch speeds and hence ranges.

Scaling the values of n to yield the same total mass fraction of gas demonstrates the importance of correctly identifying the volatile species present. For the same total amount of gas driving a steady explosive eruption, the volatiles suggested by Renggli et al. would yield pyroclast ranges (95.93/130.80 =) 73% of those we have derived from the Rutherford et al. data, whereas the Newcombe et al. inventory would imply ranges that were (322.82/130.80 =) nearly 2.5 times larger than our ranges. Neither Renggli et al. nor Newcombe et al. specifically state the mass fractions that their volatiles form of the total magma, concentrating instead on the relative speciation, but Newcombe et al. imply that they consider the equivalent magma H_2O content to be 1200 ppm, and using this to scale the other species we infer a total volatile mass fraction of ~830 ppm. Comparing this with our adopted value 3400 ppm implies that that we should multiply the above factor of~2.5 by the ratio (832/3400), reducing it to ~0.6, implying ranges that are 60% of our values. Taken together these results imply that our pyroclast ranges given in Figure 8 may be maximum estimates for common lunar magmas in relatively steady hawaiian-style eruptions. The comparison also gives an impression of the current uncertainty in predicting lunar pyroclast ranges and underlines the need for future work on the quantification of lunar magma volatile species, amounts, and release behavior as a function of pressure. Future lunar exploration, especially sample return, will provide the data needed to refine the volatile amounts and speciation needed to improve models of lunar pyroclastic eruptions. Nevertheless, the basic principles outlined here will not change, and our findings on the grain size properties of lunar pyroclastic deposits are also likely to remain essentially the same.

6.4 Implications of pyroclast morphology.

In Section 2 we used the proportions of broken glass droplets in the Apollo 17 samples (McKay et al., 1978) to estimate the pre-breakage droplet size distribution. The assemblage of intact spherical and ellipsoidal glass droplets mixed with chipped but otherwise intact droplets plus many irregular fragments strongly suggests that the source of the observed distribution was collisions between droplets that acquired their basic shapes while molten but collided after very significant cooling. Wittel et al. (2008) show that brittle failure of silicate clasts will occur at relative impact velocities greater than ~120 m s^{-1}. Figure 16 shows the paths of pyroclastic droplets ejected at a range of angles to the vertical up to our inferred limiting value of ~65 degrees when the eruption speed is 180 m s^{-1}, giving a maximum range of 20 km. Locations where droplets on different trajectories pass through the same location are identified and the relative velocities (taking account of the speed and direction of the droplets) are indicated. Clearly, droplets landing in the region extending out to about half of the maximum range are much more likely to have suffered damage than those in the distal part of the deposit. This result provides a potential method of estimating the likely distances of sampled deposits from their vents. However, this conclusion would be modified if the droplets experiencing collisions were still semi-molten at the time, underlining the need to consider the thermal history of the droplets.

6.5 Pyroclast thermal history.

In general, the pyroclastic droplets samples by the Apollo missions consist of a mixture of completely glassy droplets and droplets containing various proportions of olivine crystals (Heiken et al., 1974; McKay et al., 1978; Arndt et al., 1984; Delano, 1986). These morphologies are consistent with the cooling of the droplets at various rates (Heiken and McKay, 1978; Arndt et al., 1984; Arndt and von Engelhardt, 1987; Saal et al., 2008) as they pass through a fire fountain (Weitz et al., 1999; Renggli et al., 2017). Our droplet acceleration calculations in Section 3 allow us to track the temperature of the gas-droplet mixture for as long as there is good thermal contact between droplets and gas. For an eruption through a 3 meter radius vent, and assuming our standard 3400 ppm volatile mass fraction, the decoupling between gas and pyroclasts is complete when the mixture has expanded and cooled from its eruption temperature by 74 K over a 286 m radial distance in 1.58 seconds. The rate of temperature decrease varies from ~1000 to ~50 K s^{-1} during the expansion. By this time, all droplets are travelling on ballistic trajectories and are no longer influenced mechanically by the gas, though they can still interact thermally. For an eruption through a 20 m diameter vent, decoupling would happen after the same temperature decrease when the droplets had travelled 1.9 km in 10.5 seconds, cooling at a rate decreasing from ~150 to ~3 K s^{-1}. These model cooling rates can be compared with experimental estimates. Based on the rate of growth of olivine crystals in Apollo 17 black glass droplets, Arndt and von Engelhardt (1987) inferred that the droplets cooled at a rate less than 100 K s^{-1}. Using similar arguments, Arndt et al. (1984) found cooling rates of less than 1 K s^{-1} for Apollo 15 green glasses. For the same green glass composition, Saal et al. (2008) estimated a cooling rate of 2 to 3 K s^{-1} over ~100 to 300 s based on diffusive degassing of volatiles. We note that this time interval is similar to the travel times of droplets ejected to a maximum range of 20 km; depending on the launch angle, droplet travel times are between 94 and 222 seconds. Overall, our model values for a 20 m diameter vent match the experimental estimates more closely than our predictions for a smaller vent, but in no case do our models predict anything other than a rapidly varying cooling rate, whereas the experimental investigations appear to point to a more nearly constant rate.

These contradictions underline the problem of knowing how closely the temperatures of the pyroclasts and gas are related as the droplets travel to their final location on the ground. In many cases the droplets in Apollo samples form coherent clumps (Nagle, 1978; Marvin and Walker, 1978) suggesting that they may not have cooled completely to the ambient temperature by the time they were deposited. Droplets are so closely spaced immediately after magma fragmentation that complete opacity of the gas-droplet mixture is ensured; droplets exchange heat with one another by radiation through the gas, and a mixture of heat absorption and thermal conduction keeps the gas at the same temperature as the droplets. As droplets accelerate away from the vent and become more widely spaced, droplets near the outer edge of the resulting fountain are not completely screened from being able to radiate heat into space and so cool. The time needed to drastically cool a 2500 micron droplet able to radiate in all directions to space is ~1.5 seconds. However, a partially-shielded droplet may cool much more slowly. Wilson and Head (2017) give formulae (their equation 40 for a point source vent) for the distance inward from the outer edge of a lava fountain over which its opacity increases from zero to close to 100%. This distance is a function of the median droplet size, the maximum range of droplets, and the magma volume flux being erupted from the vent. We seek a scenario which would allow some droplets to cool relatively slowly in the opaque, inner part of a fountain and others to cool much more rapidly so that they would be prone to brittle fragmentation during collision in the outer part of the fountain. We have already seen that collisions are only energetic enough to cause brittle fracture in the inner ~50% of the deposit, so we need the translucent part of the fountain to extend inward from the outer edge at least that far. For our standard model with a maximum droplet range of 20 km, all these requirements can be satisfied if we make the opaque, hot part of the fountain extend out to about one fifth of the maximum range, i.e., to ~4 km. Equation 40 of Wilson and Head (2017) then allows us to find the erupted volume flux that produces these conditions. Figure 17 shows the relationship between the radius of the inner hot zone and the erupted volume flux for the wide range of fluxes expected in lunar volcanic eruptions. If the hot zone is to extend out no further than 4 km, the volume flux must be no more than 8.3×10^3 m^3 s^{-1}. From the spectrum of lunar mafic eruption conditions modelled by Wilson and Head (2017), a small-volume eruption fed by a dike that was only just able to penetrate the lunar crust would have this erupted volume flux if the magma at shallow depth rose at 9.5 m s^{-1} through a circular conduit of radius 16.7 m. In practice the conduit at depth would be an elongate dike and there would be some flaring outward toward the surface, but the details of the geometry do not alter the order of magnitude of the calculation.

The Wilson and Head (2017) model of fire fountain opacity focuses on the variation of number density of droplets in a fountain and does not explicitly calculate the temperatures of the droplets. The eruption model of Renggli et al. (2017, their Figure 1) attempts to do this, but assumes that each droplet carries its own parcel of gas along with it such that the temperatures of clast and gas change together as the clast cools at a fixed chosen rate of 3 K s^{-1} and the gas expands isentropically. Unfortunately, the assumption that gas and droplets stay locked together means that droplets launched at different elevations can pass through the same part of the cloud taking with them gas at different temperatures and pressures. Since the gas at any given location can have only one temperature, pressure, and travel direction, the model is not self-consistent. Clearly, developing a complete model of the structure of a fire fountain in a vacuum that includes both the hydrodynamics and thermodynamics is a vital topic for future work, bearing on volatile diffusion rates within pyroclastic droplets, nucleation and growth of phenocrysts, the ability of droplets to retain some dissolved volatiles, the condensation of volatiles from the gas phase onto the surfaces of droplets, and the possibility of droplets welding into clumps after landing.

7. Conclusions

(1) All published analyses of likely lunar volatile species suggest that some proportion of CO gas bubbles were generated and that they nucleated at much greater pressures and depths below the surface than bubbles of other volatiles released by lunar magmas. As a direct result, the total size distributions of pyroclasts produced in explosive eruptions on the Moon should be bimodal (Figure 6), with modes at ~120 and 650 microns.

(2) The expansion to extremely low pressures of the gas released in explosive eruptions on the Moon (and all other bodies with negligible atmospheres) leads to more complex interactions between the gas and pyroclasts than when a significant atmosphere is present, because the gas-particle interactions enter the Knudsen regime as the gas pressure becomes very small. This leads to the counter-intuitive finding that the median grainsize in pyroclastic deposits is expected to first increase, then decrease, and finally increase again with increasing distance from the vent (Figures 11 and 12). This is in marked contrast to the monotonic decrease with distance normally observed in explosive eruptions on Earth, and inferred for Mars.

(3) The same complex gas-particle interaction also causes the clast size distribution to vary in a complex way with distance from the vent (Figure 12) and causes the maximum thickness of the deposit to occur at about 75% of the maximum pyroclast range (Figure 13).

(4) The paucity of glass droplets larger than ~3000 microns in lunar pyroclastic deposits can be understood as being due to hydrodynamic instabilities arising from the relative velocities of liquid droplets and gas.

(5) If the inferred volatile inventory of the picritic magma that produced the orange glass beads in the Apollo 17 samples is typical of lunar magmas, maximum ranges of the bulk of the pyroclasts would have been ~20 km (Figure 8). This is consistent with the suggestion by Schmitt et al. (2019) that a fissure ~13 km from the Apollo 17 orange glass collection site is the vent for the eruption producing these pyroclasts. Similar eruptions could explain ~80% of the currently recognized pyroclastic deposits on the Moon. Since the maximum range scales essentially linearly with the total mass fraction of volatiles released, other ranges and areal coverages for other compositions can readily be predicted when more lunar magma volatile inventory data become available.

(6) Gas concentration can occur, either at the outbreak of an eruption or in its late stages. At the outbreak this is due to the accumulation of gas in the upper tip of the dike feeding the eruption that takes place during the dike's ascent from the mantle. In the late stages of an eruption it occurs as the reduced magma volume flux causes strombolian activity to replace the initial hawaiian eruption style. These gas concentration mechanisms can increase pyroclast ranges by a factor of order five, but at the expense of producing very much thinner deposits than if no gas concentration takes place. Alternatively, more moderate volatile contents coupled with low volume-flux eruptions can produce much more localized pyroclastic deposits such as the pyroclastic spatter cones with diameters up to ~10 km seen in the Marius Hills region (Head and Gifford, 1980; Lawrence et al., 2013).

(7) If all the pyroclasts in a given regional deposit originate from the same vent, there seems no alternative to the conclusion that the presence on the Moon of deposits that are both wide-spread, with radii up to at least 100 km, and voluminous, with thicknesses large enough to still be detectable spectroscopically after mixing with underlying materials during regolith formation, requires the eruption of magmas with larger total volatile contents than the ~3400 ppm maximum inferred for the Apollo 17 orange glass magma. We are currently investigating specific examples in order to assess candidate locations with greater volatile abundances.

(8) Future lunar surface exploration (human and robotic landers, rovers and sample return missions) can return essential information to improve these models and help locate candidate pyroclastic vents. Helpful information would include pyroclastic layer thickness and stratigraphic relations, pyroclastic grain-size distribution, nature of pyroclasts (e.g., glass, extent of crystallization, shape, fragmentation), surface and interior volatile content, and how all of these parameters change as a function of distance.

CRediT authorship contribution statement

Cerith Morgan: Conceptualization, Methodology, Software. **Lionel Wilson:** Conceptualization, Methodology, Software, Supervision, Writing - original draft, Funding acquisition. **James Head:** Conceptualization, Investigation, Writing - original draft, Funding acquisition.

Declaration of competing interest

The authors declare that they have no known competing financial interests or personal relationships that could have appeared to influence the work reported in this paper.

Acknowledgements

LW thanks the Leverhulme Trust for financial support though an Emeritus Fellowship, grant EM-2017-035. We gratefully acknowledge financial support from the NASA Lunar Reconnaissance Orbiter (LRO) Mission, Lunar Orbiter Laser Altimeter (LOLA) Experiment Team to JWH, grant numbers NNX09AM54G, NNX11AK29G and NNX13AO77G. We thank David Trang and an anonymous reviewer for their very helpful comments on the manuscript.

Notation

Symbol	Definition
A	Avogadro's number, 6.0225×10^{26} kmol^{-1}
C_c	Cunningham correction factor
D	magma conduit diameter
E	energy increment from gas expansion
F	gas volume fraction at start of fragmentation
G	linear growth rate of gas bubbles
H	pyroclast rise height above lava lake
Kn	Knudsen number
N	total number per unit volume of bubbles
N_f	dimensionless inverse viscosity
N_0	reference number per unit volume of bubbles
Oh	Ohnesorge number
P	pressure in magma
P_f	pressure at which fragmentation begins
P_K	pressure at onset of Knudsen effect
P_{lake}	pressure at surface of lava lake
P_{slug}	pressure in slug gas
Q	universal gas constant, 8.314 kJ kmol^{-1} K^{-1}
R	radius of magma conduit
Re	Reynolds number
T	magma eruption temperature, 1700 K
U	upward speed of gas leaving lava lake surface
U_{slug}	rise speed of slug in conduit
V	speed of pyroclasts relative to gas
We	Weber number
d	effective diameter of gas molecule, ~3-4 $\times 10^{-10}$ m
f	thickness of liquid film between slug and conduit wall
g	acceleration due to gravity, 1.62 m s^{-2}
m_k	molecular mass of *k*th volatile
n	number of gas bubbles in a given size class
$n_{f,k}$	mass fraction of the *k*th volatile at onset of fragmentation
$n_{i,k}$	mass fraction of *k*th volatile released at *i*th depth level
n_{lake}	total mass fraction of non-CO gases in lava lake
s	surface tension of magma liquid-gas interface
s_p	specific heat at constant pressure of gas
s_r	specific heat of mare basalt
s_v	specific heat at constant volume of gas
t	time scale for magma ascent
u_t	terminal velocity of a pyroclast through the gas
$v_{i,g}$	total volatile partial volume at *i*th depth level
$v_{i,l}$	liquid partial volume at *i*th depth level
$v_{i,k}$	partial volume of *k*th volatile at *i*th depth level
x	dimensionless thickness of liquid film next to slug
α	constant in energy equation
γ	effective specific heat ratio of gas-pyroclast mixture

κ	thermal diffusivity of silicate rock, ~10^{-6} m^2 s^{-1}
λ	mean free path of gas molecules
μ_g	gas viscosity
μ_l	liquid viscosity
ϕ	pyroclast diameter
φ	gas bubble diameter
ρ_l	liquid magma density
ρ_g	gas density
σ	pyroclast density
τ	pyroclast travel time

Table 1. The percentages of Apollo 17 orange glass beads found to be intact, chipped (>90% intact) or broken, as a function of size class, using data from McKay et al. (1978).

mean diameter /microns	intact droplets /%	chipped droplets /%	broken droplets /%
30.000	13.3	3.3	83.3
58.095	16.7	5.0	78.3
82.158	18.3	9.3	72.3
116.190	26.3	8.7	65.0
193.649	30.0	11.7	58.3
353.553	37.7	22.7	39.6
707.107	37.7	22.7	39.6

Table 2. Conditions at the surface of a lunar lava lake experiencing strombolian explosions as CO-dominated slugs emerge through the lake surface. The lake degasses volatiles not incorporated into the slugs in minor explosive activity approximating the behavior of a fluidized bed (see text for details). Values are given for the pressure at the base of the fluidized layer, P_{lake}, and the ejection speed, U, rise height, H, and travel time, τ, of 100-300 micron pyroclasts for a range of non-CO volatile contents, n_{lake}, up to 1000 ppm. The pressure P_{lake} provides the reference pressure for the explosions of the emerging slugs.

n_{lake} in ppm	P_{lake} in MPa	U in m s^{-1}	H in m	τ in seconds
100	0.022	7.0	15.3	8.7
200	0.044	10.0	30.6	12.3
300	0.066	12.2	45.9	15.1
500	0.111	15.7	76.5	19.4
750	0.166	19.3	114.7	23.8
1000	0.222	22.3	152.9	27.5

Table 3. Results of CO gas slugs breaking through the surface of a lava lake in strombolian explosions where the lake surface pressure is P_{lake}. In each case the pressure in the slug, P_{slug}, is given, together with the maximum and minimum effective volatile contents of the ejecta, n_{max} and n_{min}, respectively, the corresponding ejection speeds, U_{max} and U_{min}, and the corresponding ranges, R_{max} and R_{min}, on the Moon to which pyroclasts in the middle of the droplet size range could be ejected. Pressures are in Pa, volatile contents are in ppm, velocities are in m s^{-1} and ranges are in km.

(a) Conditions where no overflow of the lava lake occurs.

P_{lake}	P_{slug}	n_{max}	n_{min}	U_{max}	U_{min}	R_{max}	R_{min}
5×10^4	8.05×10^4	18174	903	353	87	77	4.7
1×10^5	1.14×10^5	25641	1866	431	128	115	10.2
1.5×10^5	1.54×10^5	34274	4603	509	198	160	24.2
2×10^5	2.00×10^5	(44009)	(34836)	(619)	(524)	(236)	(169)

(b) Conditions where copious overflow of the lava lake occurs.

P_{lake}	P_{slug}	n_{max}	n_{min}	U_{max}	U_{min}	R_{max}	R_{min}
5×10^4	3.66×10^5	77589	501	803	78	398	3.7
1×10^5	3.92×10^5	82723	559	834	92	429	5.2
1.5×10^5	4.19×10^5	87976	622	894	116	461	6.8
2×10^5	4.48×10^5	93344	692	894	116	494	8.4

Table 4. Volatile species and their molecular masses *m* in kg $kmol^{-1}$, mass fractions in the magma *n* in ppm, and ratios *n*/*m* in units of 10^6 kmol kg^{-1}, derived from the data given by the three authors specified. Mass fractions have been scaled to produce a total released magma volatile content of 3400 ppm in each case. The total of *n* and (*n*/*m*) are given at the foot of the corresponding column.

(a) Rutherford et al. (2017)

volatile	*m*	*n*	*n*/*m*
CO	28.01	1395	49.80
H_2O	18.015	1133	62.89
SO_2	64.066	327	5.10
H_2S	34.081	168	4.93
COS	60.075	327	5.44
F	18.998	50	2.63
		3400	130.80

(b) Renggli et al. (2017)

volatile	*m*	*n*	*n*/*m*
CO	28.010	860	30.69
S_2	64.130	1672	26.07
H_2	2.016	32	15.97
H_2S	34.081	510	14.96
HF	20.006	81	4.05
CS_2	76.141	105	1.38
COS	60.075	75	1.25
HS	33.073	16	0.47
HCl	36.461	13	0.36
H_2O	18.015	5	0.26
S_3	96.195	15	0.16
CO_2	44.010	7	0.15
H_2S_2	66.146	10	0.15
		3400	95.93

(c) Newcombe et al. (2017)

volatile	*m*	*n*	*n*/*m*
H_2	2.016	383	189.89
CO	28.010	1272	45.40
H_2O	18.015	1460	81.04
CO_2	44.010	289	6.49
		3400	322.82

References

Arndt, J., von Engelhardt, W., Gonzalez-Cabeza, I., Meier, B., 1984. Formation of Apollo 15 green glass beads. Proceedings of the Fifteenth Lunar and Planetary Science Conference, Part 1. Journal of Geophysical Research 89, C225–C232.

Arndt, J., von Engelhardt, W., 1987. Formation of Apollo 17 orange and black glass beads. Proceedings of the Seventeenth Lunar and Planetary Science Conference, Part 2. Journal of Geophysical Research 92(B4), E372-E376.

Barnea, D., Taitel, Y., 1993. A model for slug length distribution in gas-liquid slug flow. International Journal of Multiphase Flow 19 (5), 829–838. https://doi.org/10.1016/0301-9322(93)90046-W

Campbell, B.A., Carter, L.M., Hawke, B.R., Campbell, D.B., Ghent, R.R., 2008. Volcanic and impact deposits of the Moon's Aristarchus Plateau: a new view from Earth-based radar images. Geology 36 (2), 135–138. https://doi.org/10.1130/G24310A.1

Carey, S.N. &, Sparks, R.S.J., 1986. Quantitative models of the fallout, and dispersal of tephra from volcanic eruption columns. Bulletin of Volcanology 48, 109–125.

Carslaw, H.S., Jaeger, J.C., 1959. Conduction of Heat in Solids. 2nd edition. Oxford University Press, 510 pp.

Costello, E.S., Ghent, R.R., Lucey, P.G., 2018. The mixing of lunar regolith: vital updates to a canonical model. Icarus 314, 327-344, doi:10.1016/j.icarus.2018.05.023

Davies, R.M., Taylor, G.I., 1950. The mechanics of large bubbles rising through extended liquids and through liquids in tubes. Proceedings of the Royal Society of London A200, 375–390.

Delano, J.W., 1986. Pristine lunar glasses: criteria, data, and implications. Proceedings of the Sixteenth Lunar and Planetary Science Conference, Part 2. Journal of Geophysical Research 91 (B4), 201–213.

del Bello, E., Llewellin, E.W., Taddeucci, J., Scarlato, P., Lane, S.J., 2012. An analytical model for gas overpressure in slug-driven explosions: insights into Strombolian volcanic eruptions. Journal of Geophysical Research 117, B02206. https://doi.org/10.1029/2011JB008747

Edmonds, M., Wallace, P.J., 2017. Volatiles and exsolved vapor in volcanic systems. Elements 13, 29–34. https://doi.org/10.2113/gselements13.1.29

Farr, R.S., Groot, R.D., 2009. Close packing density of polydisperse hard spheres. Journal of Chemical Physics 131 (24), 244104. https://doi.org/10.1063/1.3276799

Fielder, G., Guest, J.E., Wilson, L., Rogers, P.S., 1967. New data on simulated lunar material. Planetary and Space Science 15 (11), 1653–1666.

Gaddis, L.R., Staid, M.I., Tyburczy, J.A., Hawke, B.R., Petro, N.E., 2003. Compositional analyses of lunar pyroclastic deposits. Icarus 161, 262–280.

Gaudin, D., Taddeucci, J., Scarlato, P., del Bello, E., Ricci, T., Orr, T., Houghton, B., Harris, A., Rao, S., A. Bucci, A., 2017. Integrating puffing and explosions in a general scheme for Strombolian-style activity. Journal of Geophysical Research - Solid Earth 122, 1860–1875. https://doi.org/10.1002/2016JB013707

Glaze, L.S., Baloga, S.M., 2000. Stochastic-ballistic eruption plumes on Io. Journal of Geophysical Research - Planets 105 (E7),17579–17588. https://doi.org/10.1029/1999JE001235

Gonnermann, H., 2015. Magma fragmentation. Annual Review of Earth and Planetary Science 43, 431–458.

Gustafson, J.O., Bell, J.F., Gaddis, L.R., Hawke, B.R., Giguere, T.A., 2012. Characterization of previously unidentified lunar pyroclastic deposits using Lunar Reconnaissance Orbiter Camera data. Journal of Geophysical Research 117, E00H25. https://doi.org/10.1029/2011JE003893

Haar, L., Gallagher, J.S., Kell, G.S., 1984. NBS/NRC Steam Tables, Hemisphere Publishing Corporation, New York, 320 pp.

Hasan, A.H., Mohammed, S.K., Pioli, L., Hewakandamby, B.N., Azzopardi, B.J., 2019. Gas rising through a large diameter column of very viscous liquid: flow patterns and their dynamic characteristics. International Journal of Multiphase Flow 116, 1–14. https://doi.org/10.1016/j.ijmultiphaseflow.2019.04.001

Hauri, E.H., Weinreich, T., Saal, A.E., Rutherford, M.C., Van Orman, J.A., 2011. High pre-eruptive water contents preserved in lunar melt inclusions. Science 333, 213–215.

Head, J.W., Gifford, A., 1980. Lunar mare domes: classification and modes of origin. The Moon and Planets 22, 235-258, doi:10.1007/BF00898434

Head, J.W., Wilson, L., 1979. Alphonsus-type dark halo craters: morphology, morphometry and eruptive conditions. Proceedings of the 10th Lunar and Planetary Science Conference, 2861–2897.

Head, J.W., Wilson, L., 1981. Lunar sinuous rille formation by thermal erosion: eruption conditions, rates and durations. Lunar and Planetary Science XII, 427–429.

Head, J.W., Wilson, L., 1989. Basaltic pyroclastic eruptions: influence of gas-release patterns and volume fluxes on fountain structure and the formation of cinder cones, spatter cones, rootless flows, lava ponds and lava flows. Journal of Volcanology and Geothermal Research 37, 261–271.

Head, J.W., Wilson, L., 1992. Magma reservoirs and neutral buoyancy zones on Venus: implications for the formation and evolution of volcanic landforms. Journal of Geophysical Research - Planets 97 (E3), 3877–3903.

Head, J.W., Wilson, L., 2017. Generation, ascent and eruption of magma on the Moon: new insights into source depths, magma supply, intrusions and effusive/explosive eruptions (Part 2: Observations). Icarus 283, 176–223. https://doi.org/10.1016/j.icarus.2016.05.031

Head, J.W., Wilson, L., 2020. Rethinking lunar mare basalt regolith formation: new concepts of lava flow protolith and evolution of regolith thickness and internal structure. Geophysical Research Letters, in press.

Head, J.W., Wilson, L., Weitz, C.M., 2002. Dark ring in southwestern Orientale basin: origin as a single pyroclastic eruption. Journal of Geophysical Research - Planets 107 (E1), 5001, 17 pp.. https://doi.org/10.1029/2000JE001438

Heiken, G.H., McKay, D.S., 1978. Petrology of a sequence of pyroclastic rocks from the valley of Taurus-Littrow (Apollo 17 landing site). Proceedings of the Lunar and Planetary Science Conference 9th, 1933-1943.

Heiken, G.H., McKay, D.S., Brown, R.W., 1974. Lunar deposits of possible pyroclastic origin. Geochimica et Cosmochimica Acta 38, 1703–1718.

Housley, R.M., 1978. Modeling lunar volcanic eruptions. Proceeding of the 9th Lunar and Planetary Science Conference, 1473–1484.

Jain, M., Prakash, R.S., Tomar, G., Ravikrishna, R.V., 2018. Secondary breakup of a drop at moderate Weber numbers. Proceedings of the Royal Society of London A471, 20130930. https://doi.org/10.1098/rspa.2014.0930

Jaupart, C., Vergniolle, S., 1988. Laboratory models of Hawaiian and Strombolian eruptions. Nature 331 (6151), 58–60. https://doi.org/10.1038/331058a0

Jaupart, C., Vergniolle, S., 1989. The generation and collapse of a foam layer at the roof of a basaltic magma chamber. Journal of Fluid Mechanics 203, 347–380. https://doi.org/10.1017/S0022112089001497

Jawin, E.R., Head, J.W., Wilson, L., 2016. Huge pyroclastic cones surrounding Cobra Head, Aristarchus Plateau: relation to Vallis Schroteri. Lunar and Planetary Science XLVII, Abstract #1505.

Jozwiak, L.M., Head, J.W., Zuber, M.T., Smith, D.E., Neumann, G.A., 2012. Lunar floor-fractured craters: classification, distribution, origin and implications for magmatism and shallow crustal structure. Journal of Geophysical Research 117, E11005. https://doi.org/10.1029/2012JE004134

Jozwiak, L.M., Head, J.W., Wilson, L., 2015. Lunar floor-fractured craters as magmatic intrusions: geometry, modes of emplacement, associated tectonic and volcanic features, and implications for gravity anomalies. Icarus 248, 424–447. https://doi.org/10.1016/j.icarus.2014.10.052

Kallmann-Bijl, H.K., 1950. Thermodynamic properties of real gases for use in high pressure problems. Research Memorandum 442, The Rand Corp., Santa Monica, CA, 44 pp., https://www.rand.org/pubs/research_memoranda/RM442.htm

Kaye G.W.C., Laby T.H., 1995. Tables of physical and chemical constants, 16th ed. London, Longman. 249 pp.

Kerber, L., Forget, F., Madeleine, J.-B., Wordsworth, R., Head, J.W., Wilson, L., 2013. The effect of atmospheric pressure on the dispersal of pyroclasts from martian volcanoes. Icarus 223, 149–156. https://doi.org/ 10.1016/j.icarus.2012.11.037

Kiefer, W.S., Macke, R.J., Britt, D.T., Irving, A.J., Consolmagno, G.J., 2012. The density and porosity of lunar rocks. Geophysical Research Letters 39, L07201. https://doi.org/ 10.1029/2012GL051319.

Kieffer, S.W., 1982. Dynamics and thermodynamics of volcanic eruptions – Implications for the plumes on Io. In: Satellites of Jupiter. Eds: Morrison, D., Shapley Matthews, M. University of Arizona Press, Tucson, AZ. 647–723.

Lawrence, S.J., Stopar, J.D., Hawke, B.R., Greenhagen, B.T., Cahill, J.T.S., Bandfield, J.L. and 8 others, 2013. LRO observations of morphology and surface roughness of volcanic cones and lobate lava flows in the Marius Hills. Journal of Geophysical Research - Planets 118, 615-634, doi:10.1002/jgre.20060

Li, S., Milliken, R.E., 2017. Water on the Moon as seen by the Moon Mineralogy Mapper: distribution, abundance and origins. Science Advances 3, 1–11. https://doi.org/ 10.1126/sciadv.1701471

Lister, J.R., 1990a. Buoyancy-driven fluid fracture - the effects of material toughness and of low-viscosity precursors. Journal of Fluid Mechanics 210, 263–280.

Lister, J.R., Kerr, R.C., 1991. Fluid-mechanical models of crack-propagation and their application to magma transport in dykes. Journal of Geophysical Research 96 (B6), 10,049–10,077.

Llewellin, E.W., del Bello, E., Taddeucci, J., Scarlato, P., Lane, S.J., 2012. The thickness of the falling film of liquid around a Taylor bubble. Proceedings of the Royal Society A 468, 1041–1064. https://doi.org/10.1098/rspa.2011.0476

Lowenstern, J.B., 2001. Carbon dioxide in magmas and implications for hydrothermal systems. Mineralium Deposita 36, 490–502.

Mangan, M.T., Cashman, K.V., 1996. The structure of basaltic scoria and reticulite and inferences for vesiculation, foam formation, and fragmentation in lava fountains. Journal of Volcanology and Geothermal Research 73, 1–18.

Marvin, U.B., Walker, D., 1978. Implications of a titanium-rich glass clod at Oceanus Procellarum. American Mineralogist 63, 924-929.

Masotta, M., Keppler, H.Ni.H., 2014. In situ observations of bubble growth in basaltic, andesitic and rhyodacitic melts. Contributions to Mineralogy and Petrology 167, 976. https://doi.org/10.1007/s00410-014-0976-8

McKay, D.S., Heiken, G.H., Waits, G., 1978. Core 74001/2: Grain size and petrology as a key to the rate of in situ reworking and lateral transport on the lunar surface. Proceedings of the Lunar and Planetary Science Conference 9th, 1913-1932, Lunar and Planetary Institute, Houston.

Milliken, R.E., Li, S., 2017. Remote detection of widespread indigenous water in lunar pyroclastic deposits. Nature Geoscience 10, 561–565.

Morgan, C.R., Wilson, L., Head, J.W., 2019. Factors controlling the size distributions of lunar pyroclasts. Lunar and Planetary Science 50, abstract #1341.

Nagle, J.S., 1978. Drive-tubes 74002/74001:Dissection and description. Lunar Core Catalog, NASA Johnson Space Center, Houston, Supplement, 49 pp.

Newcombe, M.E., Brett, A., Beckett, J.R., Baker, M.B., Newman, S., Guan, Y., Eiler, J.M., Stolper, E.M., 2017. Solubility of water in lunar basalt at low pH_2O. Geochimica et Cosmochimica Acta 200, 330–352.

NIST, 2018. U.S. National Institute of Standards and Technology Standard Reference Database Number 69. https://doi.org//10.18434/T4D303, visited at https://webbook.nist.gov/chemistry/ on 11 June 2020.

Parfitt, E.A., 2004. A discussion of the mechanisms of explosive basaltic eruptions. Journal of Volcanology and Geothermal Research 134 (1–2), 77–107. https://doi.org/10.1016/j.jvolgeores.2004.01.002

Parfitt, E.A., Wilson, L., 1995. Explosive volcanic-eruptions - IX: The transition between Hawaiian-style lava fountaining and Strombolian explosive activity. Geophysical Journal International 121 (1), 226–232. https://doi.org/10.1111/j.1365-246X.1995.tb03523.x

Pering, T.D., McGonigle, A.J.S., 2018. Combining spherical-cap and Taylor bubble fluid dynamics with plume measurements to characterize basaltic degassing. Geosciences 8, 42, 14 pp. https://doi.org/10.3390/geosciences8020042

Qiao, L., Head, J.W., Ling, Z., Wilson, L., Xiao, L., Dufek, J.D., Yan, J., 2019. Geological characterization of the Ina shield volcano summit pit crater on the Moon: evidence for extrusion of waning-stage lava lake magmatic foams and anomalously young crater retention ages. Journal of Geophysical Research - Planets 124, 1100-1140. https://doi.org/10.1029/2018JE005841

Renggli, C.J., King, P.L., Henley, R.W., Norman, M.D., 2017. Volcanic gas composition, metal dispersion and deposition during explosive volcanic eruptions on the Moon. Geochimica et Cosmochimica Acta 206, 296–311.

Rubin, A.M., 1993. Dikes vs. diapirs in viscoelastic rock. Earth and Planetary Science Letters 119, 641–659.

Rutherford, M.J., Head, J.W., Saal, A.E., Hauri, E., Wilson, L., 2017. Model for the origin, ascent and eruption of lunar picritic magmas. American Mineralogist 102, 2045–2053. https://doi.org/10.2138/am-2017-5994ccbyncnd

Saal, A.E., Hauri, E.H., Lo Cascio, M., Van Orman, J.A., Rutherford, M.C., Cooper, R.F., 2008. Volatile content of lunar volcanic glasses and the presence of water in the Moon's interior. Nature 454 (7201), 192–195.

Sarda, P., Graham, D., 1990. Mid-ocean ridge popping rocks: implications for degassing at ridge crests. Earth and Planetary Science Letters 97, 268–289.

Sato, M., 1977. Driving mechanism of lunar pyroclastic eruptions inferred from oxygen fugacity behavior of Apollo 17 orange glass. Transactions of the American Geophysical Union 58(6), 425-425.

Schmitt, H.H., Petro, N.E., Wells, R.A., Robinson, M.S., Weiss, B.P., Mercer, C.M., 2017. Revisiting the field geology of Taurus-Littrow. Icarus 298, 2-33, doi:10.1016/j.icarus.2016.11.042

Shearer, C.K., Hess, P.C., Wieczorek, M.A., Pritchard, M.E., Parmentier, E.M., Borg, L.E. and 10 others, 2006. Thermal and magmatic evolution of the Moon. Reviews in Mineralogy and Geochemistry 60, 365-518, doi:10.2138/rmg.2006.60.4

Smorygo, O., Mikutski, V., Marukovich, A., Ilyushchanka, A., Sadykov, V., Smirnova, A., 2011. An inverted spherical model of an open-cell foam structure. Acta Materialia 59 (7), 2669–2678. https://doi.org/10.1016/j.actamat.2011.01.005

Speyerer, E.J., Povilaitis, R.Z., Robinson, M.S., Thomas, P.C., Wagner, R.V., 2016. Quantifying crater production and regolith overturn on the Moon with temporal imaging. Nature 538 (7624), 215-218, doi:10.1038/nature19829

Strom, R.G., Terrile, R.J., Masursky, H., Hansen, C., 1979. Volcanic eruption plumes on Io. Nature 280 (5725), 733–736. https://doi.org/10.1038/280733a0

Strom, R.G., Schneider, N.M., Terrile, R.J., Cook, A.F., Hansen, C., 1981. Volcanic-eruptions on Io. Journal of Geophysical Research - Space Physics 86, 8593–8620. https://doi.org/10.1029/JA086iA10p08593

Suckale, J., Hager, B.H., Elkins-Tanton, L.T., Nave, J.-C., 2010. It takes three to tango: 2. Bubble dynamics in basaltic volcanoes and ramifications for modeling normal strombolian activity. Journal of Geophysical Research 115, B07410. https://doi.org/10.1029/2009JB006917

Taddeucci, J., Edmonds, M., Houghton, B., James, M.R., Vergniolle, S., 2015. Hawaiian and strombolian eruptions. Ch. 27, pp. 485-503 in The Encyclopedia of Volcanoes, Ed. H. Sigurdsson, Academic Press. https://doi.org/10.1016/B978-0-12-385938-9.00027-4

Trang, D., Gillis-Davis, J.J., Lemelin, M., Cahill, J.T.S., Hawke, B.R., Giguere, T.A., 2017. The compositional and physical properties of localized lunar pyroclastic deposits. Icarus 283, 232–253. https://doi.org/10.1016/j.icarus.2016.09.025

Vergniolle, S., Jaupart, C., 1986. Separated two-phase flow and basaltic eruptions. Journal of Geophysical Research 91 (B12), 12,842–12,860. https://doi.org/10.1029/JB091iB12p12842

Wang, C.J., Peterson, J.B., 1957. Spreading of supersonic jets from axially-symmetric nozzles. The Ramo-Wooldridge Corporation, Los Angeles, CA., internal report, downloaded 8 April 2020 from https://hdl.handle.net/2027/coo.31924004612788

Weitz, C.M., Rutherford, M.J., Head, J.W., McKay, D.S., 1999. Ascent and eruption of a lunar high-titanium magma as inferred from the petrology of the 74001/2 drill core. Meteoritics and Planetary Science 34(4), 527-540, doi:10.1111/j.1945-5100.1999.tb01361.x

Wieczorek, M.A., Neumann, G.A., Nimmo, F., Kiefer, W.S., Taylor, G.J., Melosh, H.J., Phillips, R.J., Solomon, S.C., Andrews-Hanna, J.C., Asmar, S.W., Konopliv, A.S., Lemoine, F.G., Smith, D.E., Watkins, M.M., Williams, J.G., Zuber, M.T., 2013. The crust of the Moon as seen on GRAIL.

Science 339, 671–675. https://doi.org/ 10.1126/science.1231530

Williams, D.A., Fagents, S.A., Greeley, R., 2000. A reevaluation of the emplacement and erosional potential of turbulent, low-viscosity lavas on the Moon. Journal of Geophysical Research 105, 20,189–20,206.

Wilson, L., 1999. Explosive Volcanic Eruptions - X. The influence of pyroclast size distributions and released magma gas contents on the eruption velocities of pyroclasts and gas in hawaiian and plinian eruptions. Geophysical Journal International 136 (3), 609–619.

Wilson, L., Head, J.W., 1981. Ascent and eruption of basaltic magma on the Earth and Moon. Journal of Geophysical Research 86 (B4), 2971–3001.

Wilson, L., Head, J.W., 2003. Deep generation of magmatic gas on the Moon and implications for pyroclastic eruptions. Geophysical Research Letters 30, (12), 1605, 4 pp. https://doi.org/10.1029/2002GL016082

Wilson, L., Head, J.W., 2007. Explosive volcanic eruptions on Mars: tephra and accretionary lapilli formation, dispersal and recognition in the geologic record. Journal of Volcanology and Geothermal Research 163, 83–97. https://doi.org/ 10.1016/j.jvolgeores.2007.03.007

Wilson, L., Head, J.W., 2017a. Generation, ascent and eruption of magma on the Moon: new insights into source depths, magma supply, intrusions and effusive/explosive eruptions (Part 1: Theory). Icarus 283, 146–175. https://doi.org/10.1016/j.icarus.2015.12.039

Wilson, L., Head, J.W., 2017b. Eruption of magmatic foams on the Moon: formation in the waning stages of dike emplacement events as an explanation of "Irregular Mare Patches". Journal of Volcanology and Geothermal Research 335, 113–127. https://doi.org/10.1016/j.volgeores.2017.02.009

Wilson, L., Head, J.W., 2018a. Lunar floor-fractured craters: modes of dike and sill emplacement and implications of gas production and intrusion cooling on surface morphology and structure. Icarus 305,105–122. https://doi.org/10.1016/j.icarus.2017.12.030

Wilson, L., Head, J.W., 2018b. Controls on lunar basaltic volcanic eruption structure and morphology: gas release patterns in sequential eruption phases. Geophysical Research Letters 45 (12), 5852–5859. https://doi.org/10.1029/2018GL078327

Wilson, L., Heslop, S.,1990. Clast sizes in terrestrial and martian ignimbrites. Journal of Geophysical Research 95 (B11), 17309–17314.

Wilson, L., Walker, G.P.L., 1987. Explosive volcanic eruptions - VI. Ejecta dispersal in plinian eruptions: the control of eruption conditions and atmospheric properties. Geophysical Journal of the Royal Astronomical Society 89 (2), 657–679.

Wilson, L., Head, J.W., Zhang, F., 2019. A theoretical model for the formation of ring moat dome structures: products of second boiling in the distal parts of lunar basaltic lava flows. Journal of Volcanology and Geothermal Research 374, 160–180. https://doi.org/10.1016/j.jvolgeores.2019.02.018

Wittel, F.K., Carmona, H.A., Kun, F., Herrmann, H.J., 2008. Mechanisms in impact fragmentation. International Journal of Fracture 154(1),105-117, doi:10.1007/s10704-008-9267-6

Xia, G.-D., Cui, Z.-Z., Liu, Q., Zhou, F.-D., Hu, M.-S., 2009. A model for liquid slug length distribution in vertical gas-liquid slug flow. Journal of Hydrodynamics 21 (4), 491–498. https://doi.org/10.1016/S1001-6058(08)60175-4

Figures and Captions.

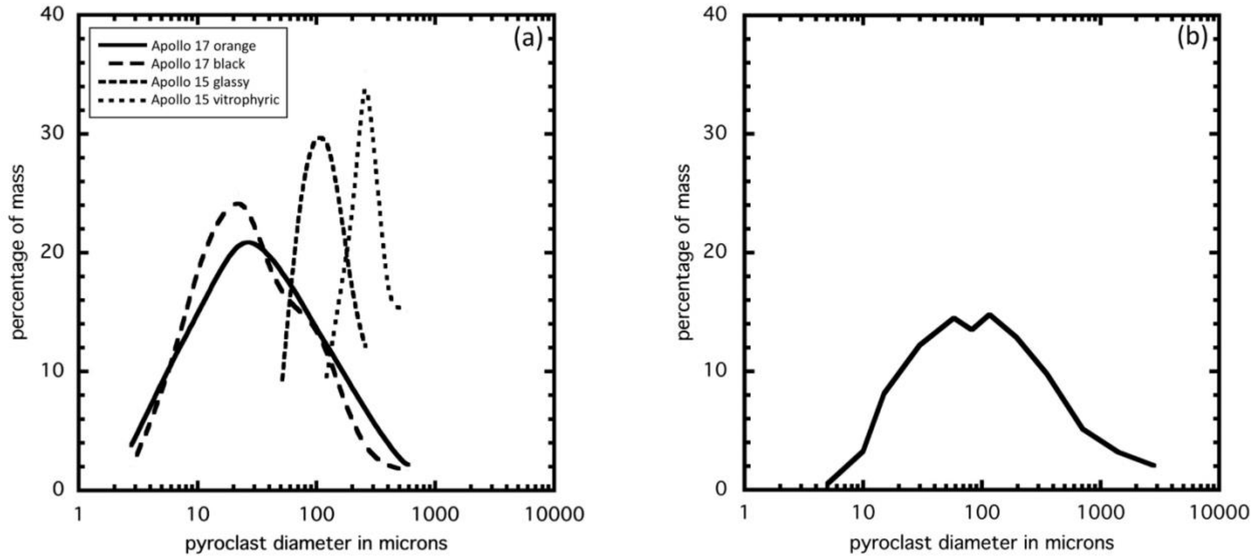

Figure 1. (a) Distribution by mass of pyroclastic glass beads as a function of size in two Apollo 17 samples (Heiken et al., 1974) and an Apollo 15 sample (Arndt et al., 1984). (b) Reconstruction of original size distribution of Apollo 17 orange glass beads based on bead breakage data in McKay et al. (1978).

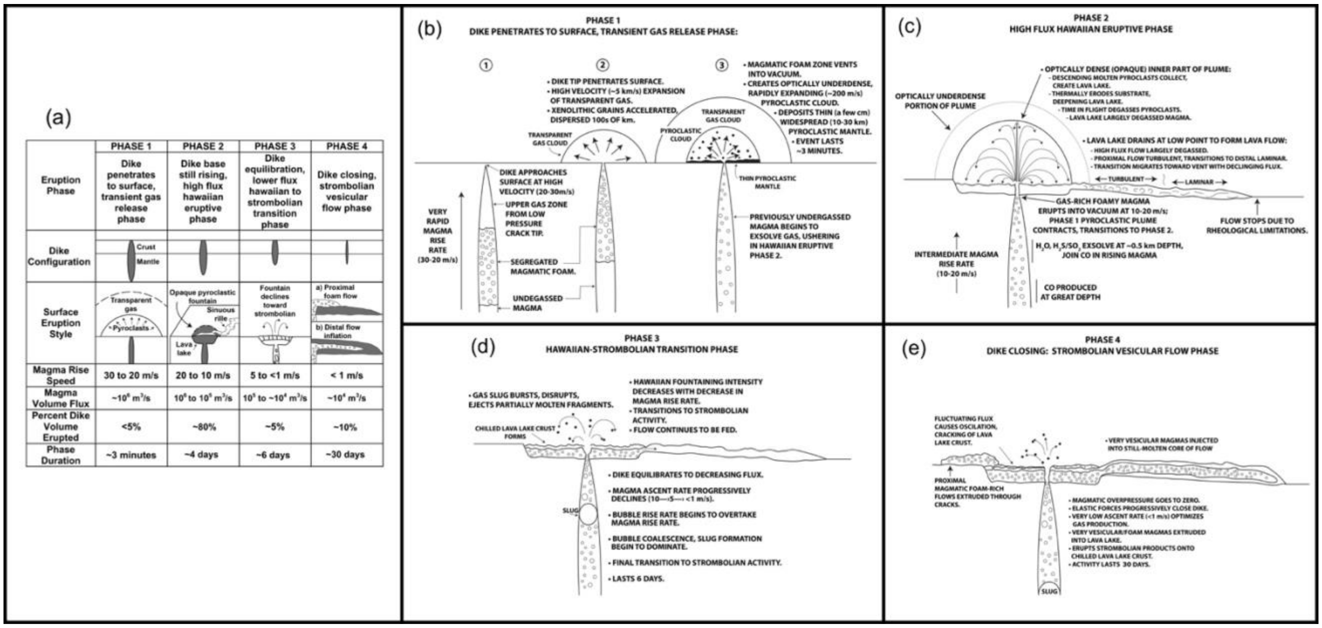

Figure 2. (a) Variation of various relevant parameters with time during the four phases of the development of a typical long-duration eruption on the Moon: (b) Initial transient release, as dike breaches the surface, of gas accumulated in top of dike during its ascent; (c) high magma volume flux hawaiian phase; (d) hawaiian to strombolian transition phase as volume flux decreases; (e) final strombolian phase at low magma rise speed as dike closes and cools. Based on Figure 1 in Wilson and Head (2018b).

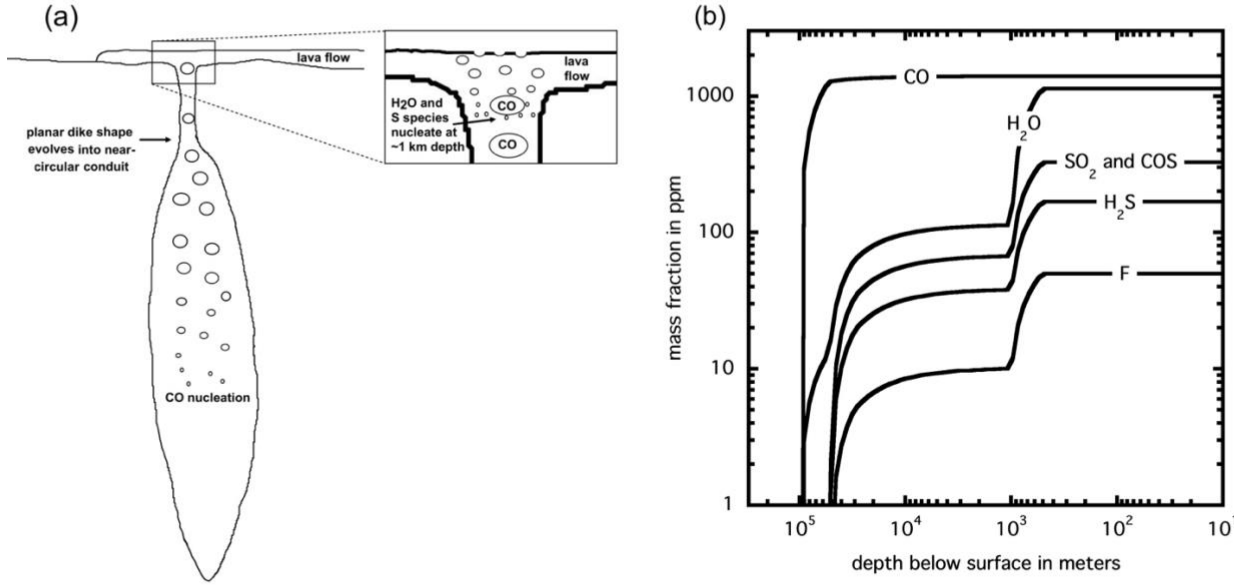

Figure 3. Pattern of release of volatiles during the steady ascent of the picritic lunar magma described by Rutherford et al. (2017). (a) Conceptual diagram of the geometry of the dike and vent system showing where volatile release occurs. Relative bubble sizes indicated; absolute sizes and depths not to scale. (b) The mass fraction of each species present as gas bubbles as a function of depth below the surface.

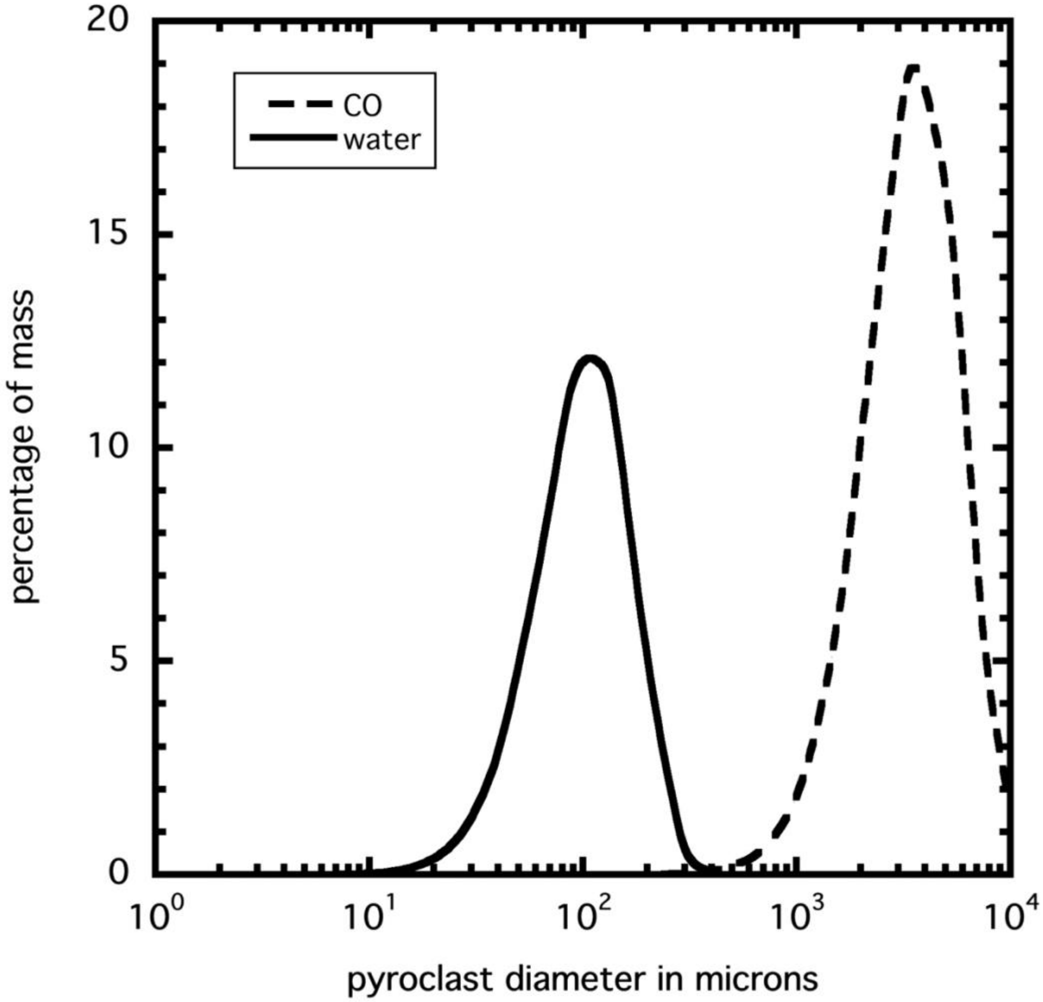

Figure 4. Distribution by mass of pyroclastic glass beads predicted on the basis of a simple model of gas bubble growth during steady eruptions in which the bubbles containing CO released at great depth and bubbles containing H_2O and sulfur compounds do not interact as they reach dense packing near the surface.

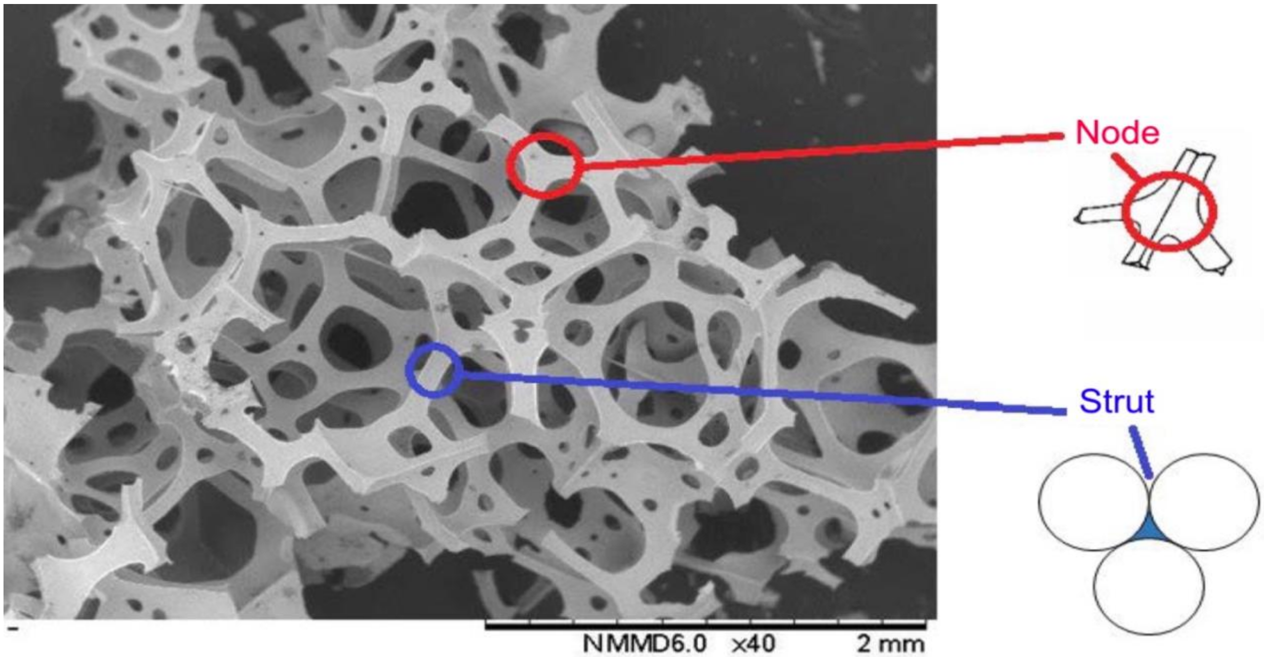

Figure 5. Electron-micrograph of a section of a reticulite clast from the Pu'u 'O'o eruption of Kilauea volcano, Hawai'i. Using the strut and node terminology from Smorygo et al. (2011), the image shows how small bubbles occupy the nodes between large bubbles in close packing, thus interfering with the droplet size distribution produced when struts between nodes collapse. Image courtesy of Cardiff Catalysis Institute.

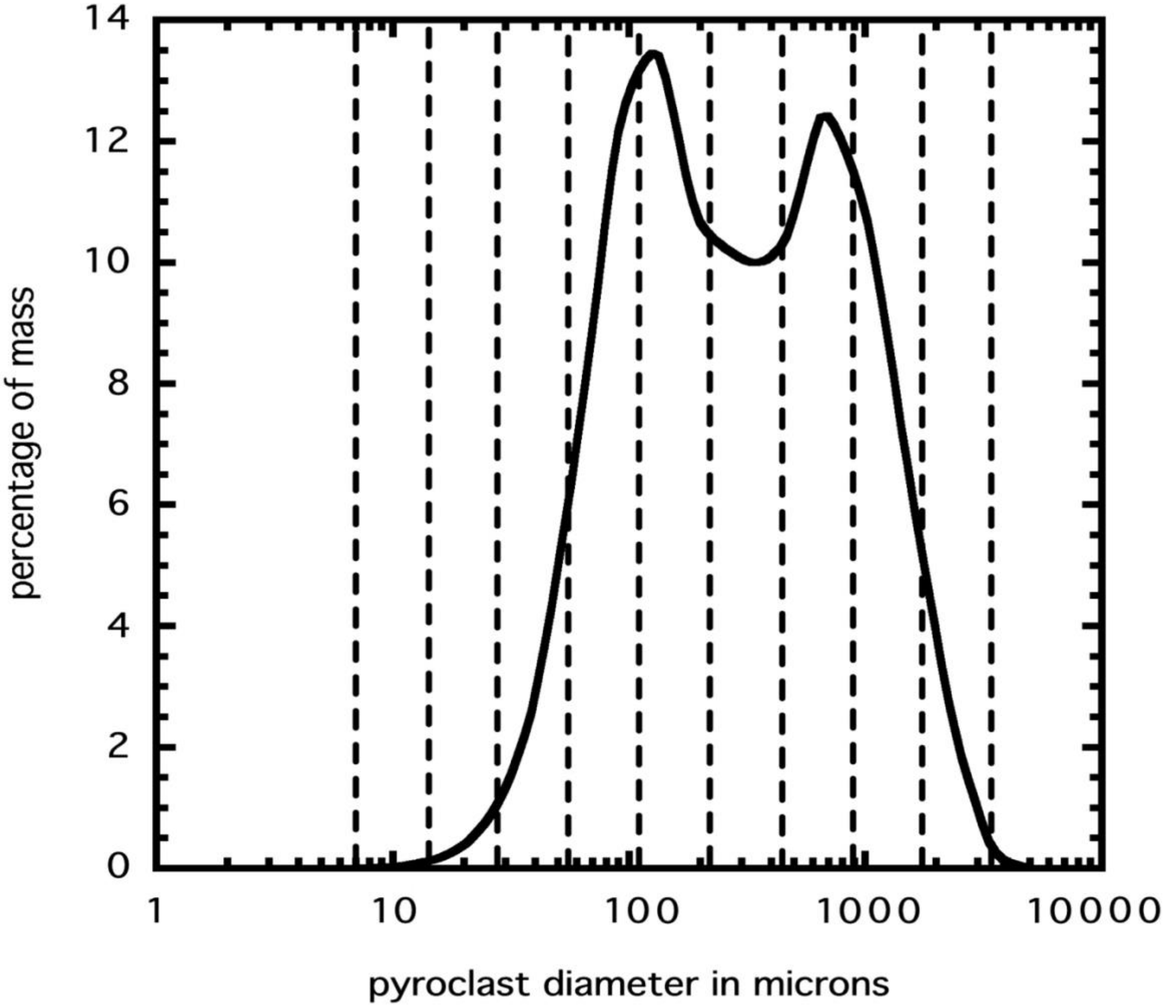

Figure 6. Distribution by mass of pyroclastic glass beads produced in steady hawaiian-style eruptions predicted by modifying Figure 4 using measurements on the image shown in Figure 5 to estimate the pattern of the disruption of nodes between large bubbles by the collapse of small bubbles. The vertical broken lines subdivide the distribution into size classes for later use.

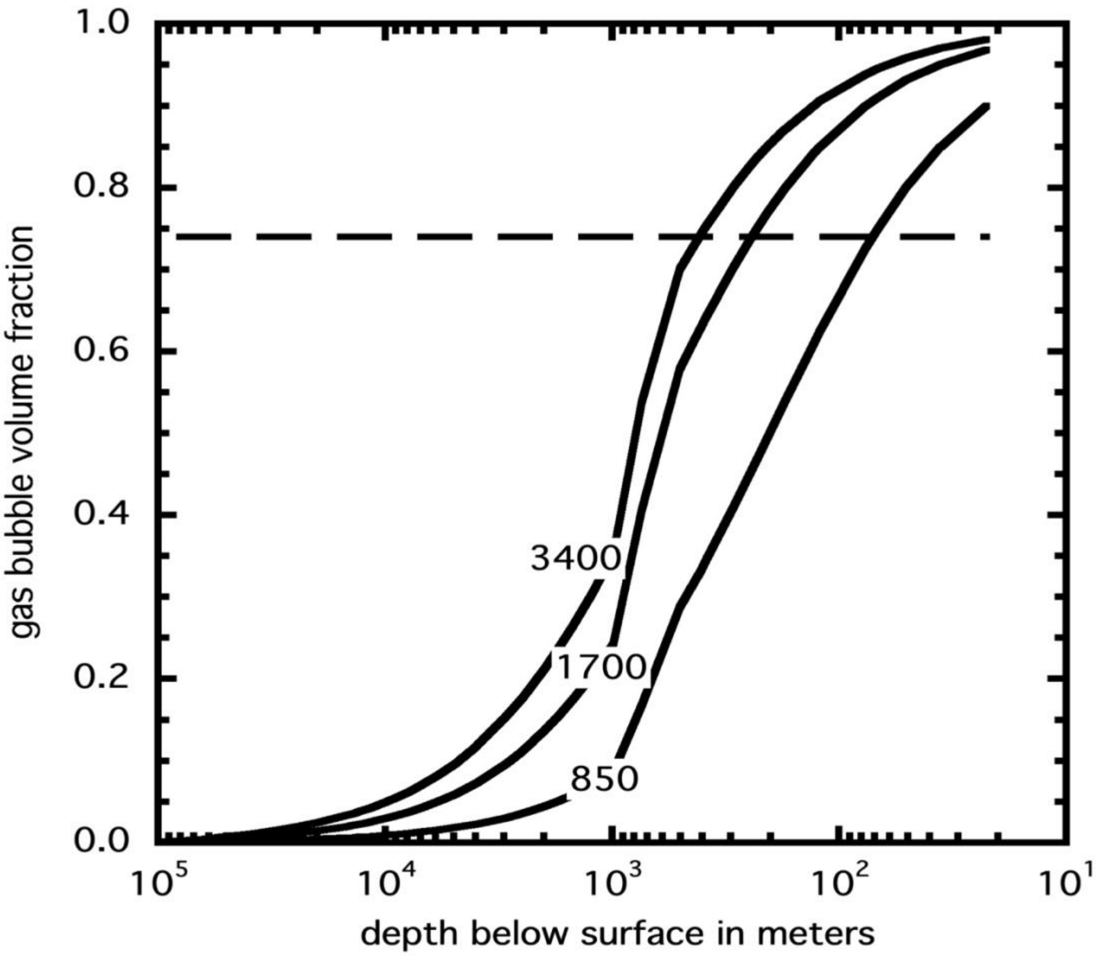

Figure 7. Variation of the total volume of gas bubbles as a function of depth below the surface in the magma whose volatile release pattern is shown in Figure 3b. The curve labeled 3400 corresponds to the total 3400 ppm volatile content of this magma; the curves labeled 1700 and 850 represent the equivalent bubble concentrations in magmas with one half and one quarter, respectively, of the magma studied. The dashed line represents the critical gas bubble volume fraction, 0.74, for the onset of magma fragmentation deduced by applying the analysis of Farr and Groot (2009).

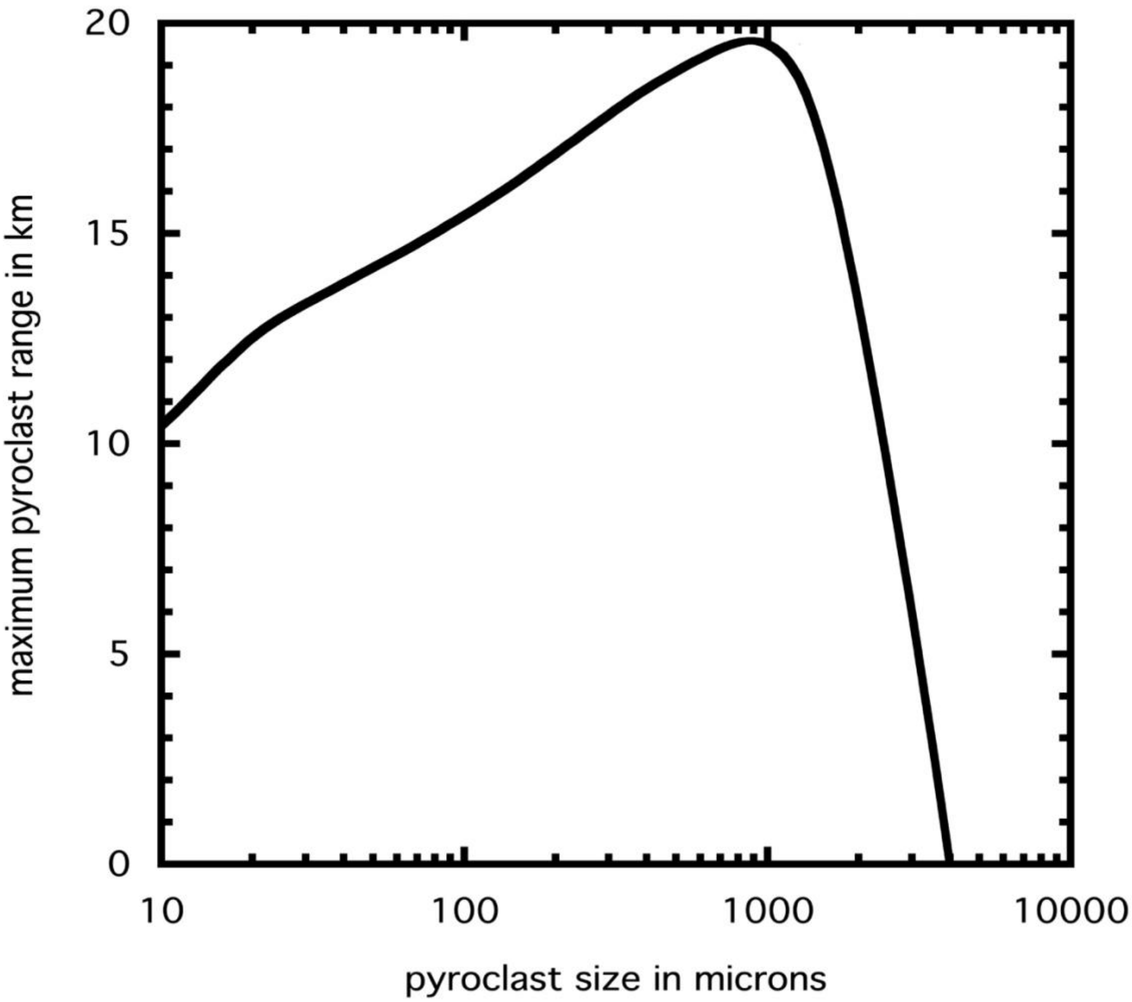

Figure 8. Maximum radial distance from the vent that can be reached by pyroclasts of a given diameter in steady hawaiian-style eruptions when the total magma volatile content is 3400 ppm.

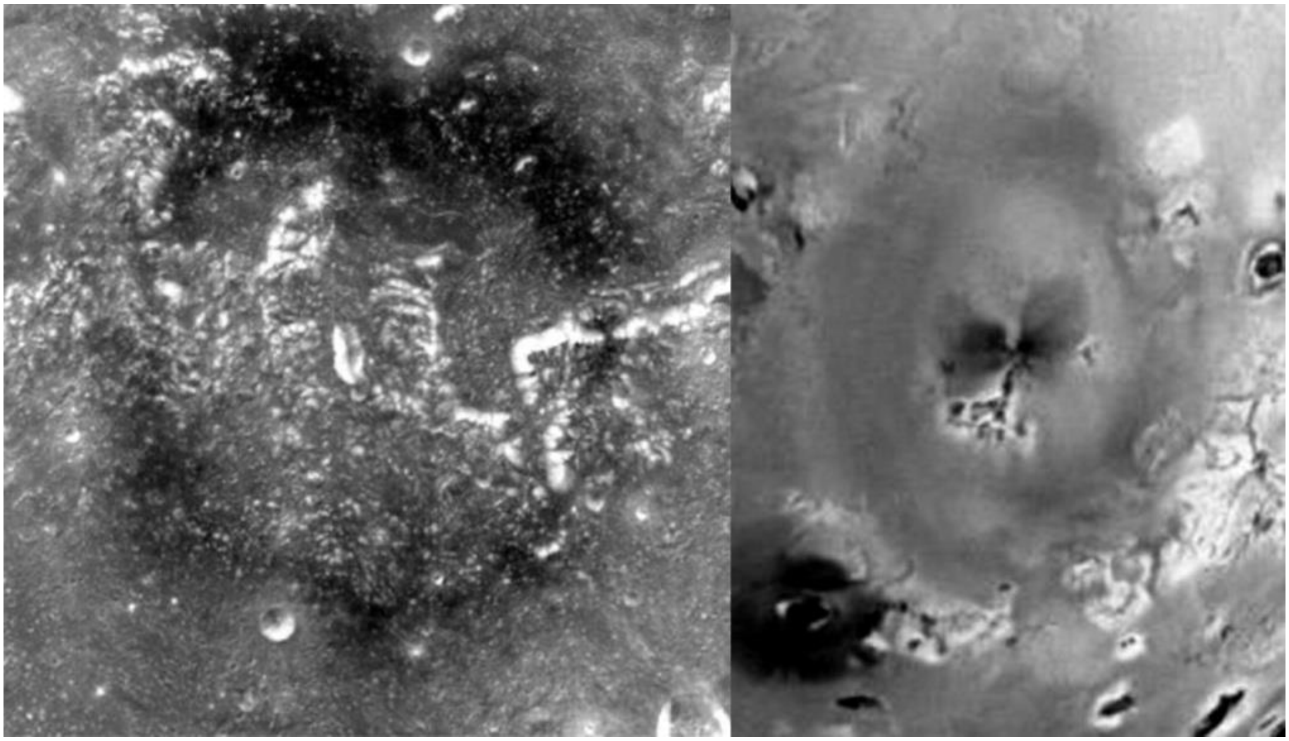

Figure 9. Examples of pyroclastic deposits showing evidence for a concentration of ejecta near the maximum range from the vent. Left image: the ~150 km diameter dark ring deposit in the Orientale basin interior analyzed by Head et al. (2002); Right image: an ~1000 km diameter deposit from an eruption of Pele volcano on Io. Part of NASA PhotoJournal image PIA00738 based on Galileo orbit G7 imaging data. North is at the top in both images.

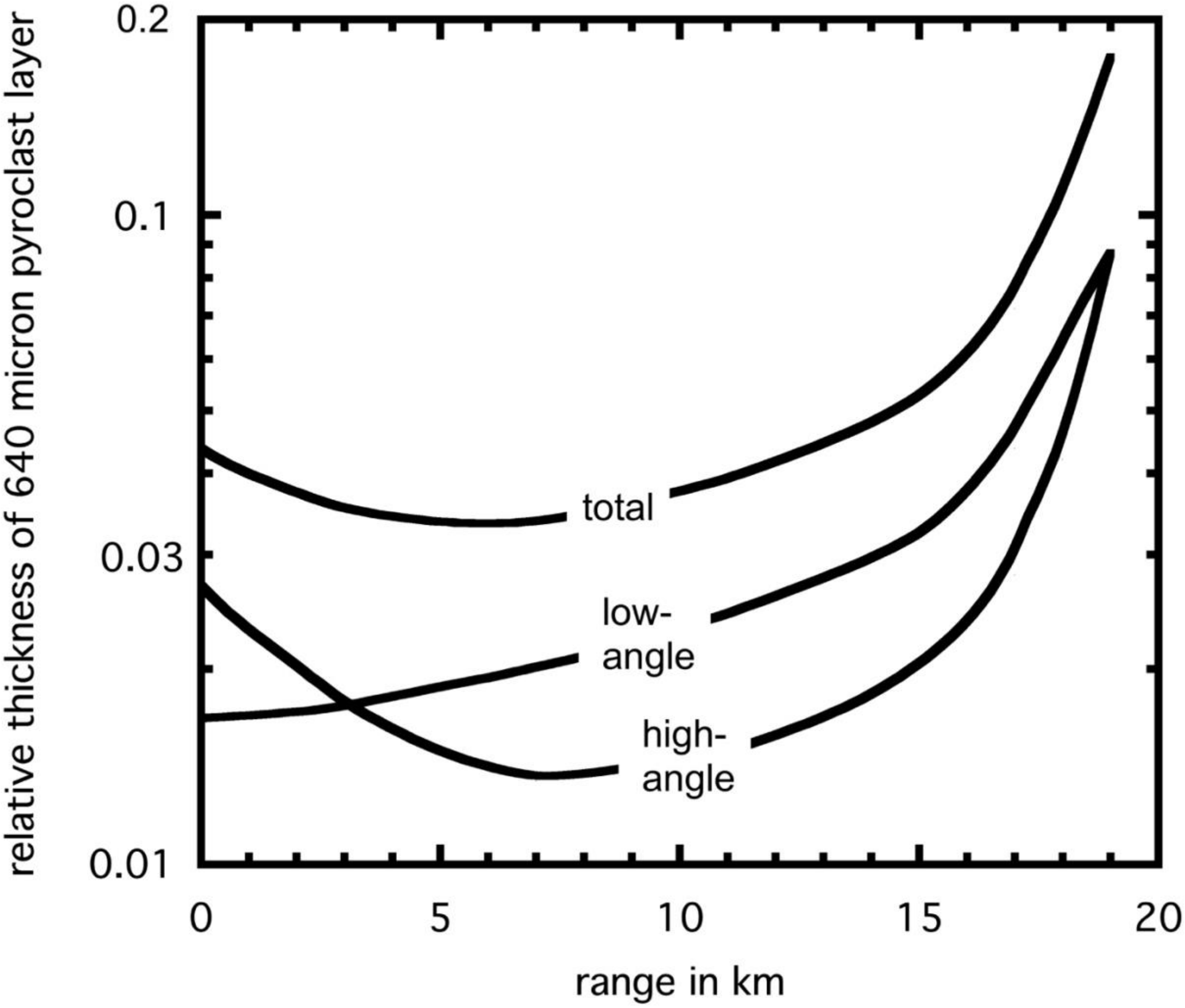

Figure 10. Relative thickness as a function of radial distance from the vent of the layer of pyroclasts formed by clasts that travel by high angle and low angle paths, respectively, to reach a given range, together with the total thickness. The curves shown are for the 640 micron size class indicated in Figure 6, but the pattern is similar for all size classes.

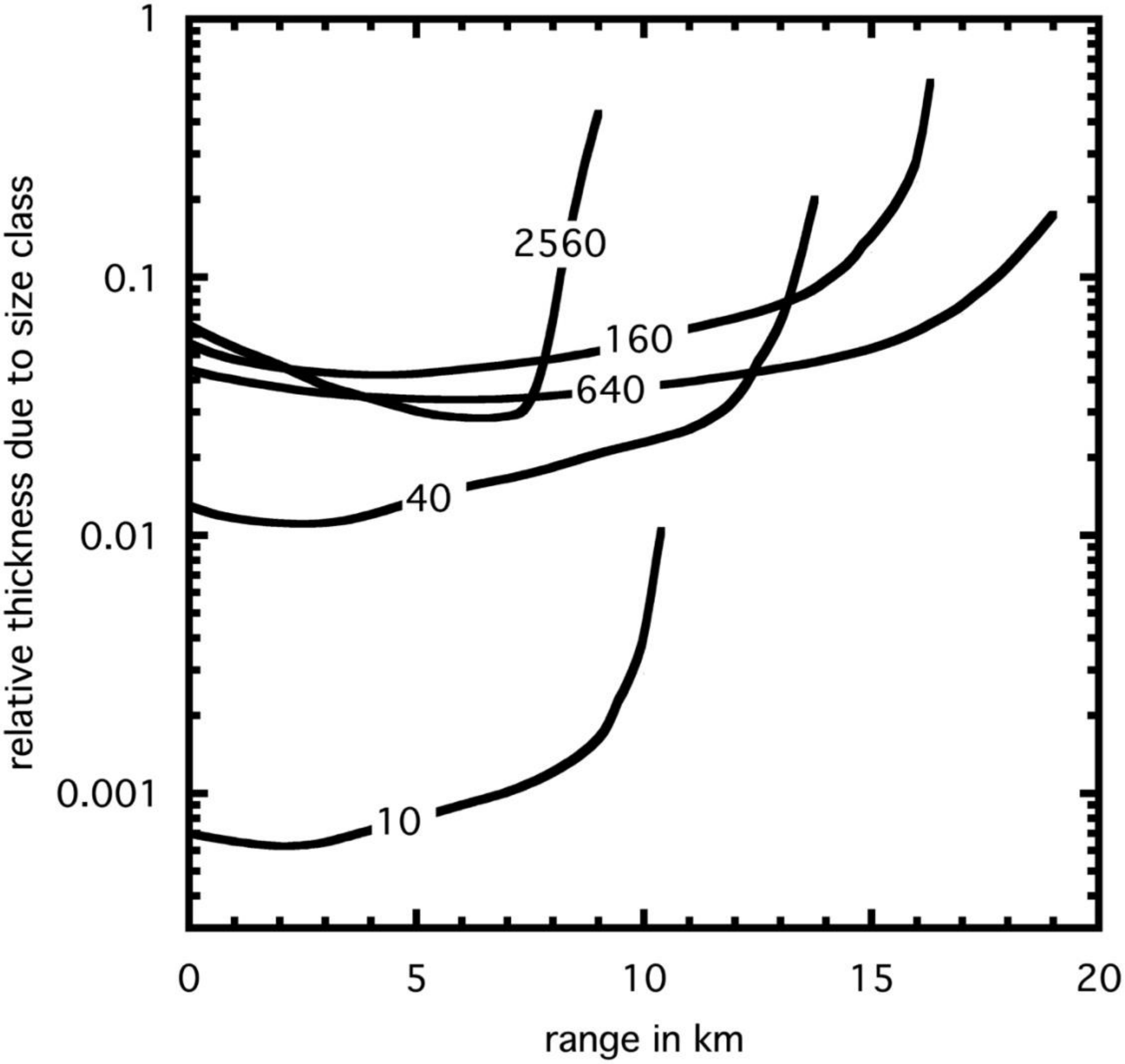

Figure 11. Relative thickness as a function of radial distance from the vent of the pyroclast layers due to 5 of the 9 size classes modeled. Other size classes show analogous patterns. Curves are truncated at the maximum range reached by clasts of the stated size (curve labels in microns).

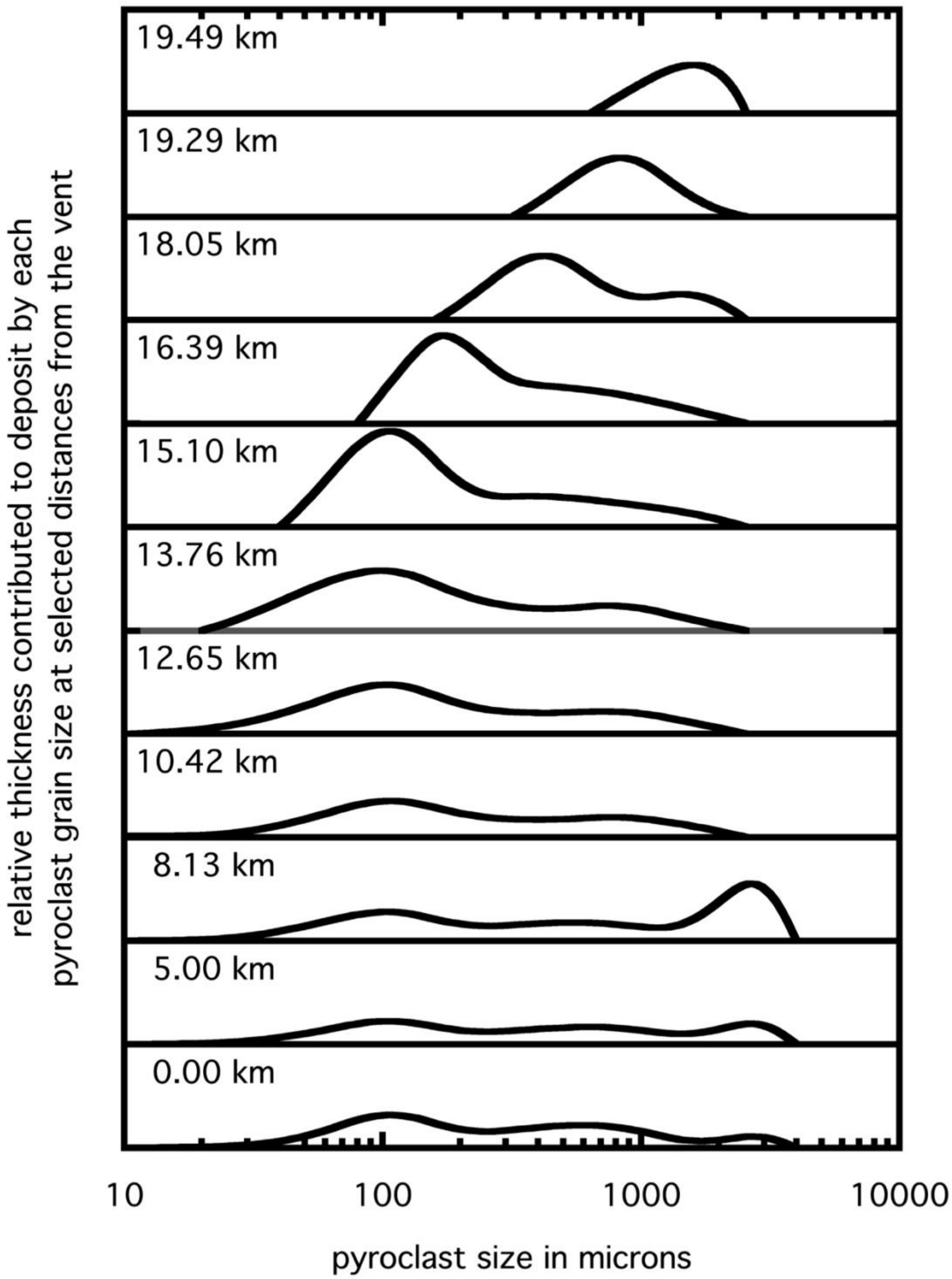

Figure 12. Grain size distribution of pyroclasts in a deposit at a series of 11 radial distances from the vent. These are distributions by mass, and assume that the deposit has the same bulk density at all locations, so that the curves also represent the relative thickness of the deposit contributed by each grain size class at the stated range.

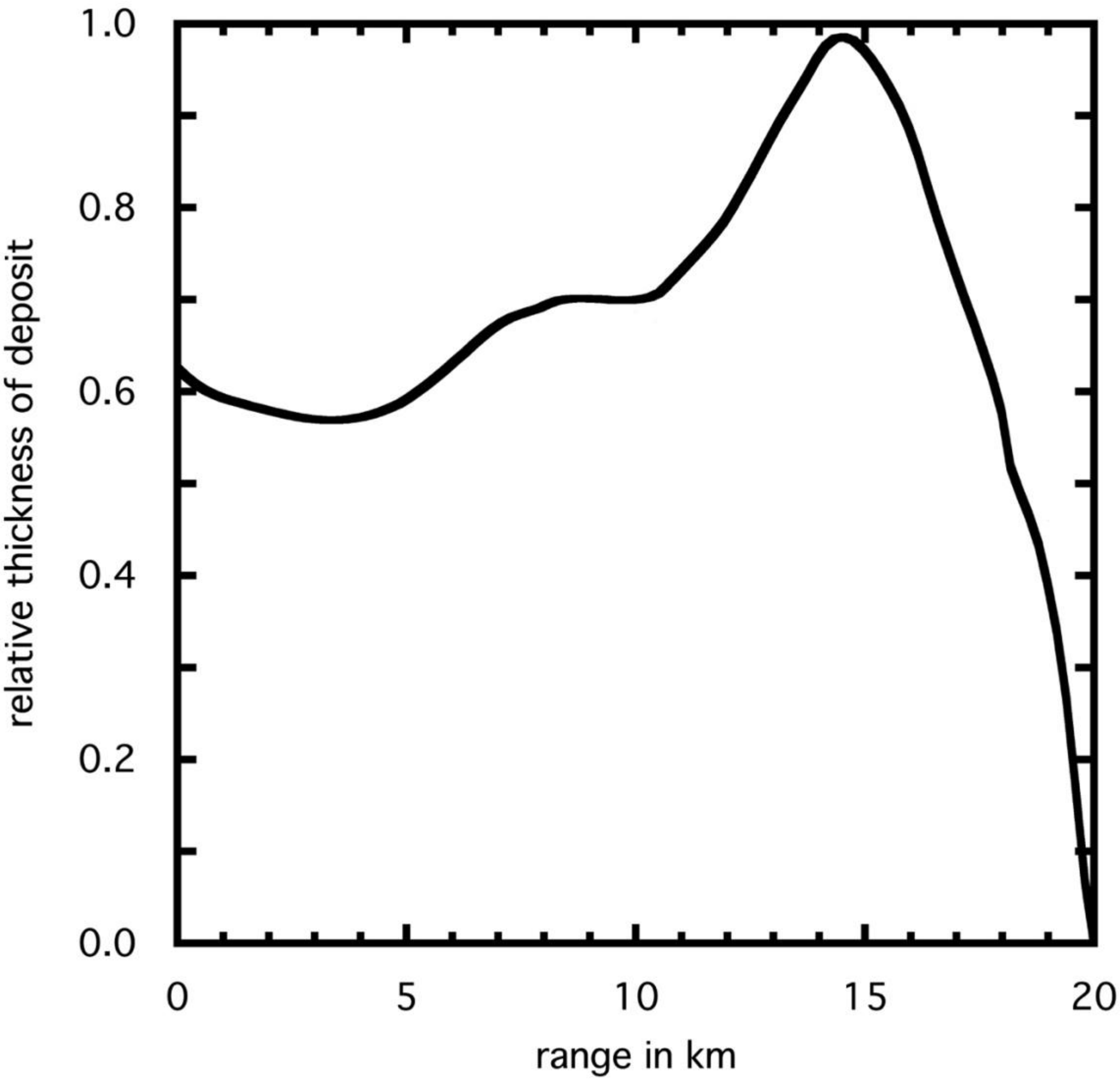

Figure 13. Variation with radial distance from the vent of the total thickness of the deposit, obtained by summing the contributions at each radial distance from all of the grain size classes. A significant increase in thickness occurs at distances around 75% of the maximum range. There is little suggestion of an edifice immediately surrounding the vent.

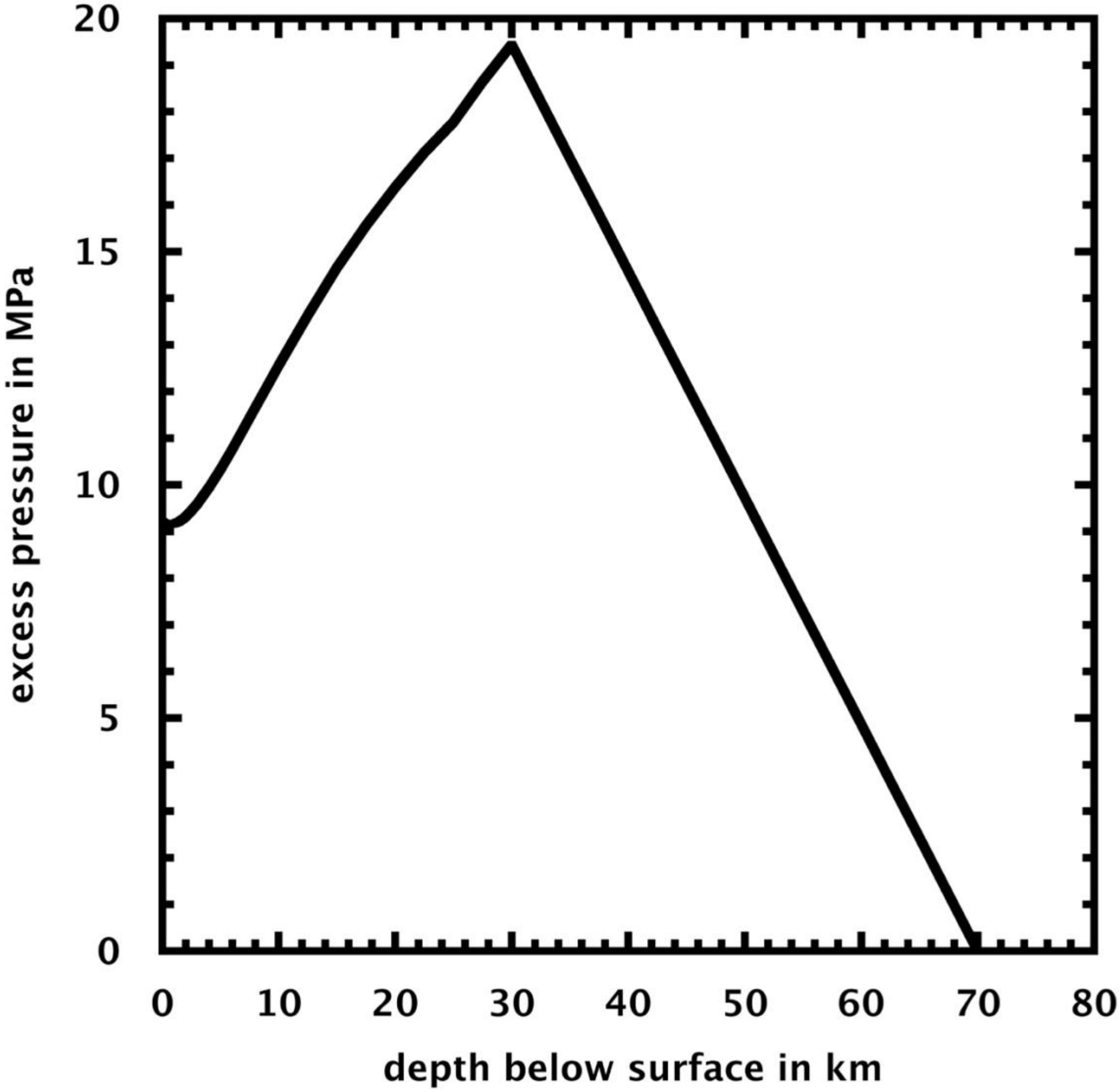

Figure 14. Excess pressure as a function of depth in the magma in a dike that has penetrated close to the surface without erupting and has accumulated CO gas bubbles in its upper part. The dike extends from the surface to a depth of 70 km; CO bubbles released at depths down to 50 km have accumulated into the upper 25 km of the dike, increasing the gas mass fraction in that region from an initial 1395 ppm (Figure 3b) to 2790 ppm. The excess pressure is a maximum at the crust-mantle boundary and has reached 5.8 MPa close to the surface. If this dike now begins to erupt into the lunar vacuum, a transient eruption occurs as magma decompresses explosively from the 5.8 MPa level releasing 2790 ppm of CO together with all of the other five volatiles shown in Figure 3b, which together amount to 2005 ppm, making a total of 4795 ppm gas driving a significantly more energetic eruption than if no gas concentration had occurred.

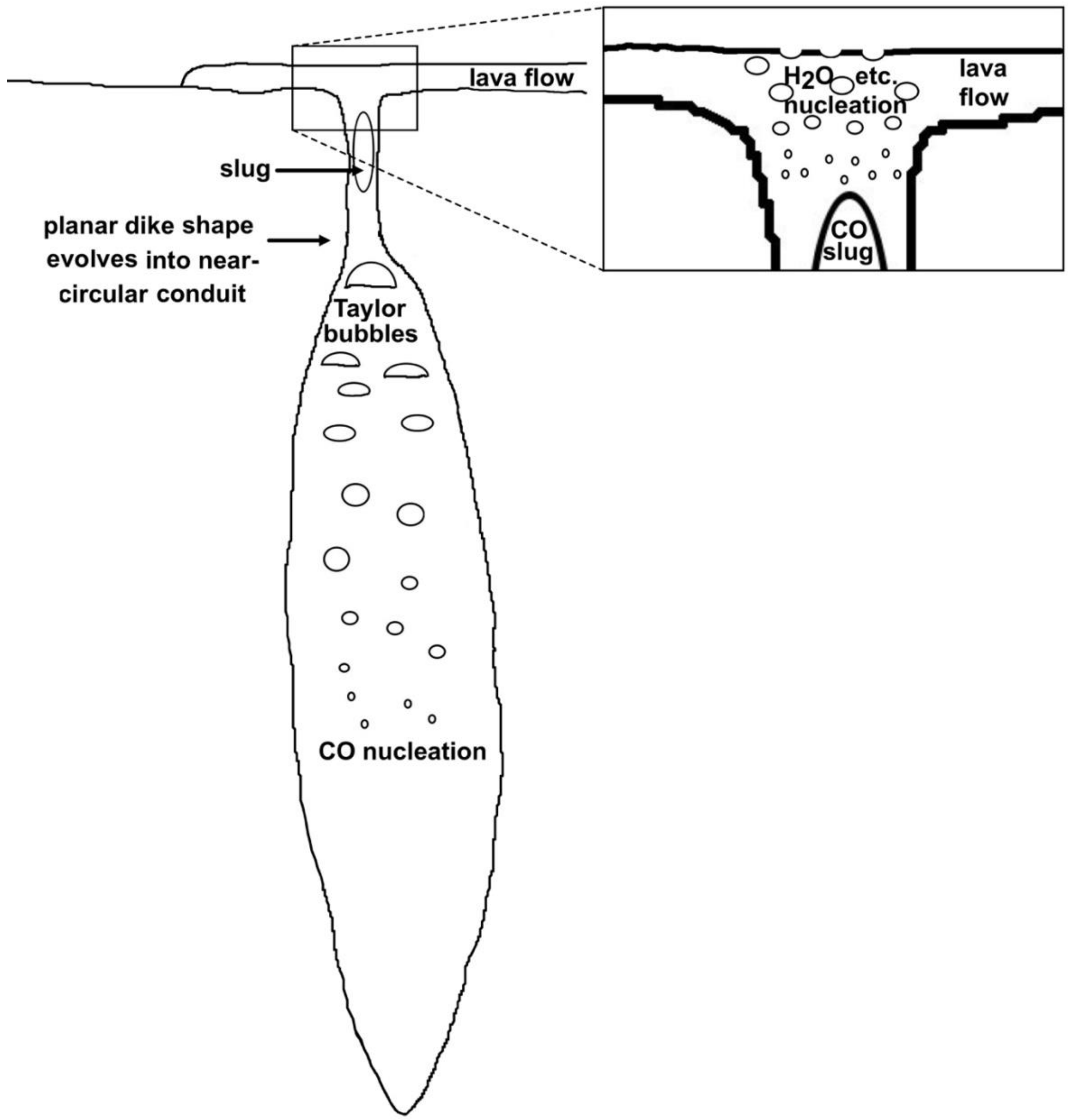

Figure 15. Conceptual diagram of deep nucleation, growth and coalescence of CO bubbles leading to the formation of Taylor bubbles and eventually slugs ascending into the conduit connecting a dike to a lava pond at the surface. Inset shows shallow generation of bubbles of H_2O and sulfur compounds. The slugs burst through the surface of the vesicular lava lake surrounding the vent to produce a strombolian explosion. Relative bubble sizes indicated; absolute sizes and depths not to scale.

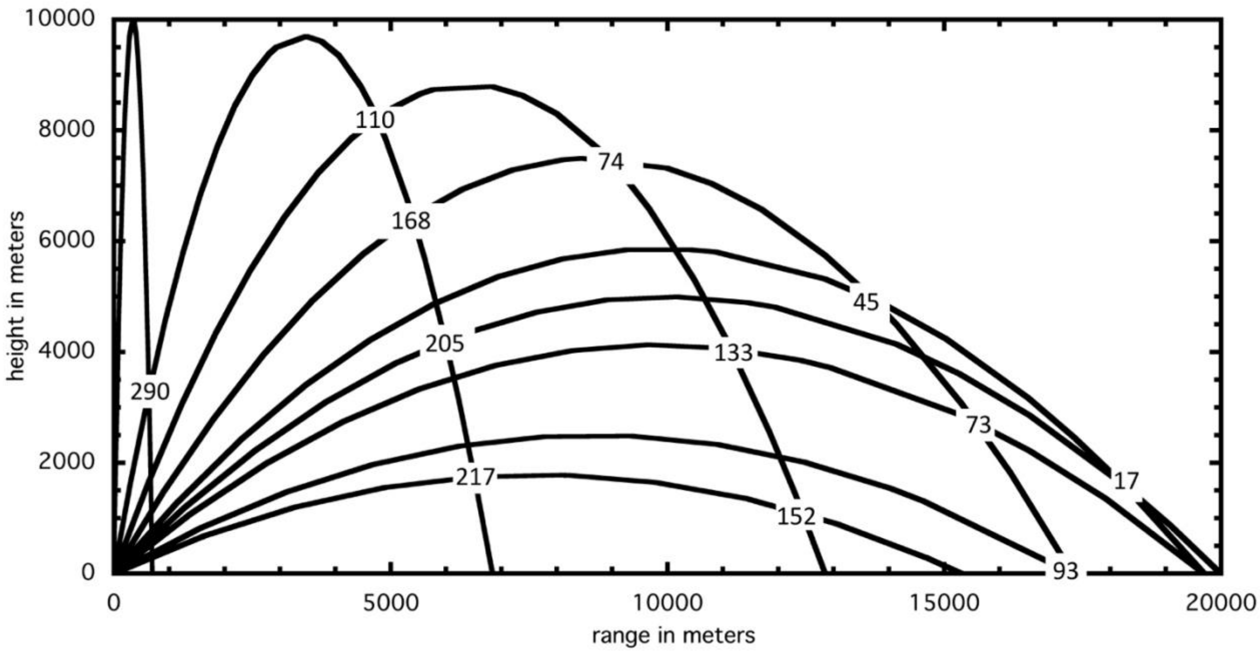

Figure 16. Trajectories of a series of pyroclastic droplets ejected from the vent at angles of 1, 10, 20, 30, 40, 45, 50, 60 and 65 degrees from the vertical. Ejection speed is 180 m s^{-1} leading to a maximum range of 20 km. Twelve examples of locations where droplet collisions can occur are shown and the superposed number is the relative speed in m s^{-1} of clasts colliding at that point. Wittel et al. (2008) show that brittle fracture is likely at collision speeds greater than 120 m s^{-1}, implying that breakage will be greatest in the proximal half of the deposit.

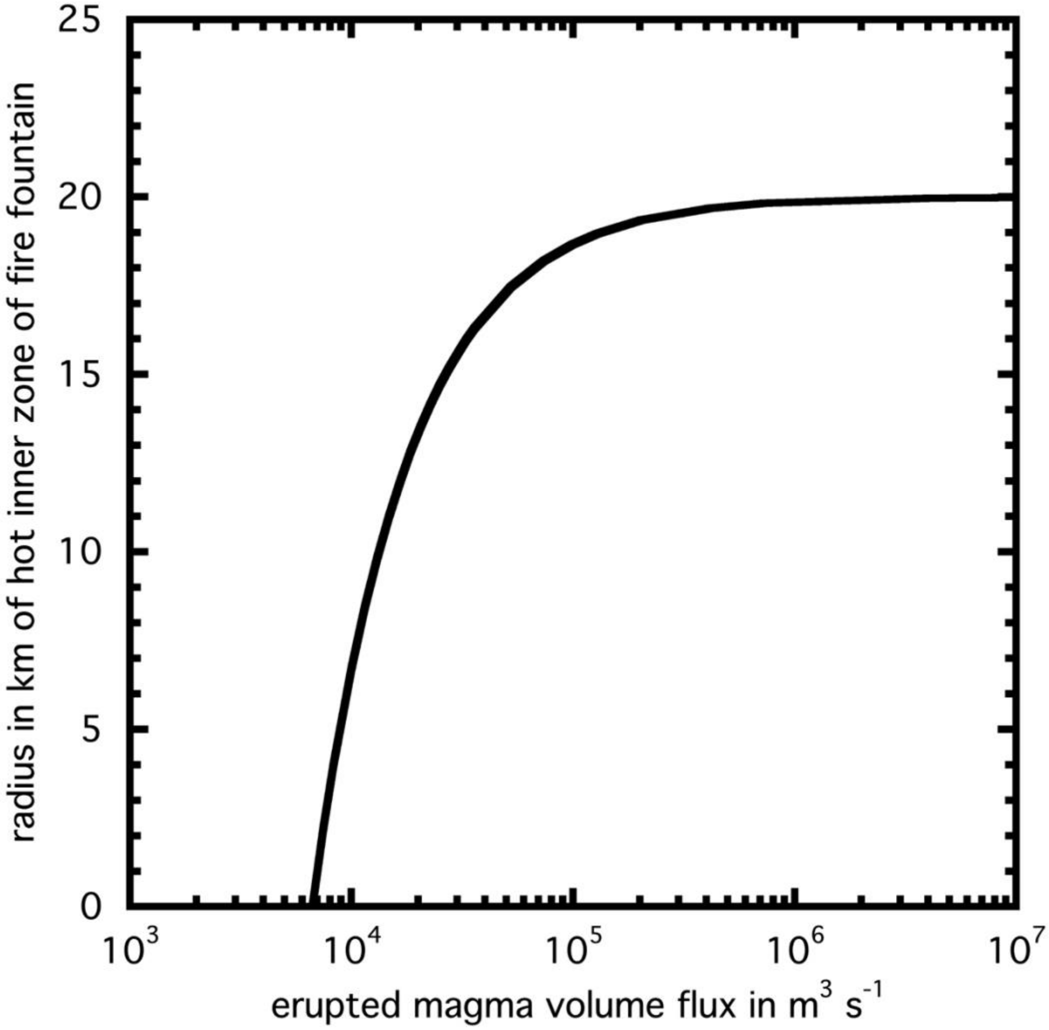

Figure 17. The radius of the hot inner zone of a lunar fire fountain as a function of the volume flux of magma rising to the surface for an eruption where the total magma volatile content is 3400 ppm and the maximum pyroclast range is 20 km.